

Unveiling the main sequence of galaxies at $z \geq 5$ with the James Webb Space Telescope: predictions from simulations

Jordan C. J. D’Silva,^{1*} Claudia D. P. Lagos,^{1,2,3} Luke J. M. Davies,¹ Christopher C. Lovell,⁴
Aswin P. Vijayan^{3,5}

¹International Centre for Radio Astronomy Research (ICRAR), M468, University of Western Australia, 35 Stirling Hwy, Crawley, WA 6009, Australia

²ARC Centre of Excellence for All Sky Astrophysics in 3 Dimensions (ASTRO 3D).

³Cosmic Dawn Center (DAWN).

⁴Centre for Astrophysics Research, School of Physics, Astronomy & Mathematics, University of Hertfordshire, Hatfield AL10 9AB, UK.

⁵DTU-Space, Technical University of Denmark, Elektrovej 327, DK-2800 Kgs. Lyngby, Denmark

Accepted XXX. Received YYY; in original form ZZZ

ABSTRACT

We use two independent, cosmological galaxy formation simulations, FLARES, a hydrodynamical simulation, and SHARK, a semi-analytic model, to explore how well the James Webb Space Telescope (JWST) will be able to uncover the existence and parameters of the star-forming main sequence (SFS) at $z = 5 \rightarrow 10$, i.e. shape, scatter, normalisation. Using two independent simulations allows us to isolate predictions (eg. stellar mass, star formation rate, SFR, luminosity functions) that are robust to or highly dependent on the implementation of the physics of galaxy formation. Both simulations predict JWST to be able to observe every intrinsically bright galaxy up to $z \sim 10$ (down to stellar masses of $\approx 10^{8.3} M_{\odot}$ and SFRs of $\approx 1 M_{\odot} \text{ yr}^{-1}$) in modest integration times. JWST will therefore be able to accurately constrain the parameters of the SFS given current proposed survey areas (e.g. the Webb COSMOS 0.7 deg^2). Although both simulations predict qualitatively similar distributions of stellar mass and SFR, there are important quantitative differences, such as the abundance of massive, star-forming galaxies (with FLARES predicting a higher abundance than SHARK); the early onset of quenching as a result of black hole growth in FLARES (at $z \approx 8$), not seen in SHARK until much lower redshifts; and the effect of chemical enrichment upon the observed light from galaxies (with FLARES predicting much less dust attenuation compared to SHARK that that we attribute to SHARK’s quick metal enrichment). JWST observations will allow us to distinguish between these models, leading to a significant improvement upon our understanding of the formation of the very first galaxies.

Key words: cosmology:theory – galaxies:star formation – galaxies:high redshift – infrared:JWST

1 INTRODUCTION

A ubiquitous feature of galaxies is the tight coupling between star formation rates (SFR) and stellar masses that has been observed to exist out to high redshifts with very little scatter over the breadth of the SFR – M_{\star} plane (Brinchmann et al. 2004; Salim et al. 2007; Noeske et al. 2007b,a; Whitaker et al. 2012a); the so called star forming main sequence (SFS). To first order $\text{SFR} \propto M_{\star}^{\alpha}$ where α is a constant; though, differing opinions exist in the literature as to whether the SFS is best described as a single component power law model (e.g. Wuyts et al. 2011; Whitaker et al. 2012b; Speagle et al. 2014; Pearson et al. 2018) or a two component power law model (e.g. Lee et al. 2015; Leslie et al. 2020; Thorne et al. 2021). Two component functions model the low and high stellar mass end of the SFS separately to account for distinct slopes in these mass regimes, which accordingly trace different populations of galaxies (Whitaker et al. 2012a). The use of a double power law function to describe the SFS is motivated by a turn over in the SFS that has been shown to occur for massive galaxies on the SFR – M_{\star} plane that experience

a downturn toward lower SFRs away from a linear trend (Abramson et al. 2014; Cook et al. 2020). The physical mechanism behind the SFS and its low scatter is believed to be that galaxies relax toward the locus of the SFS by the internal and self-consistent regulation of star formation. The inflow rate of gas that is needed for star formation is in equilibrium with a combination of the rate at which stars are being formed and the rate at which gas is diverted from the galaxy via outflows driven by feedback from stars, supernovae and active galactic nuclei (e.g. Lilly et al. 2013; Tacchella et al. 2016). This equilibrium needs to be quickly regained when galaxies are thrown out of it to explain the tightness of the SFS. Indeed, this has been demonstrated to be the case in simulations (e.g. Schaye et al. 2010; Lagos et al. 2011, 2014; Matthee & Schaye 2019).

Stellar masses and SFRs have been previously determined out to $z \sim 8$ (Bouwens et al. 2015; González et al. 2011; Katsianis et al. 2017) with instruments like the Advance Camera for Surveys on board the Hubble Space Telescope (HST; Beckwith et al. 2006; Koekemoer et al. 2007; Grogin et al. 2011). The trouble with these results is that they are generally short wavelength surveys that can be complicated by the effect of dust attenuation (Draine 2003). The results of these surveys are sensitive to the methods that are used

* E-mail: 22252335@student.uwa.edu.au

to correct for dust attenuation. This is particularly problematic as it is unclear whether dust obscured galaxy populations have been robustly accounted for, which have shown to become dominant at $z \sim 1 - 2$ (Casey et al. 2014). At higher redshifts, it is unclear whether dust-obscured galaxies can make a significant contribution to the cosmic SFR density or not (e.g. Casey et al. 2018.) Sub-millimetre (sub-mm) instruments, like the Atacama Large Millimetre Array (ALMA), have been able to constrain the sub-mm emission of hundreds of galaxies (Fudamoto et al. 2021) at $z > 1$, and as sub-mm light is the result of the dust re-radiating absorbed short wavelength photons, these measurements can be used to constrain the SFRs of these galaxies. The problem with these observations is two fold. First, ALMA has a small field-of-view, and hence it could potentially be missing a number of intermediate-to-bright sub-mm bright galaxies, if their frequency is rare, leading to systematic uncertainties in the estimated cosmic SFR density of more than a factor of 2 at $z \geq 4$ (Casey et al. 2018). Second, it is difficult to determine stellar masses from sub-mm observations (Michałowski et al. 2014). While studies have attempted to confirm the existence of the SFS at $z \geq 5$, the stellar mass range is too small (< 1 dex) to obtain meaningful measurements of the slope and scatter of the SFS (Pearson et al. 2018; Leslie et al. 2020; Thorne et al. 2021), and the UV rest-frame wavelengths used to measure stellar masses can be extremely affected by dust attenuation. This is about to dramatically change, thanks to the recently launched James Webb Space Telescope (JWST; Gardner et al. 2006), which is observing in the infrared ($\lambda \sim 0.5 \rightarrow 30.0\mu\text{m}$), with exquisite resolution and sensitivity. Infrared photons are far less easily attenuated by intervening dust because the average grain size is smaller by diameter than infrared wavelengths (Mathis et al. 1977). The Near Infrared Camera (NIRCam) on board the JWST is an order of magnitude more sensitive and covers a greater area per pointing than the already existing infrared capabilities of the Wide Field Camera 3 on board the HST (Gardner et al. 2006). A key goal of the JWST is to provide a complete census of galaxies out to $z \sim 10$.

A key outcome of new observations is to confirm or challenge the current understanding of astrophysical processes. It is thus important to produce tailored predictions for what the JWST will be able to uncover as it continues to observe the distant Universe. For this, we can turn our attention to physically motivated galaxy formation models. Galaxy formation simulations have a rich history (eg. Somerville & Davé 2015), and have proven to be a vital tool for interpreting and predicting physical observations of the Universe, especially those from large multi-wavelength galaxy surveys (Cole et al. 2000; Baugh 2006; Benson 2010; Vogelsberger et al. 2014; Schaye et al. 2015; Croton et al. 2016; Lagos et al. 2018). In order to make meaningful predictions for the JWST, these simulations must include a description of galaxy formation in combination with a description of the spectral output of those simulated galaxies to directly test possible biases affecting the observations.

In this work we use state-of-the-art simulations to address whether the JWST will be able to predict the existence, and properties, of the SFS from $z = 5 \rightarrow 10$. Recent studies have explored JWST predictions (Vogelsberger et al. 2020; Shen et al. 2021; Curtis-Lake et al. 2021; Wilkins et al. 2022a,b,c), mostly focusing on luminosity functions (LF) and expected numbers of galaxies. In addition, these generally present predictions within an individual model, without exploring the dependence of their predictions on the details of galaxy formation modelling. In this work instead, we make use of two independent galaxy formation models, using drastically different techniques, the cosmological hydrodynamical simulation suite FLARES (Lovell et al. 2021; Vijayan et al. 2021), and the semi-analytic model of galaxy formation SHARK (Lagos et al. 2018), with the aim of iso-

lating predictions that appear robust to the details of the models, and those that are highly model dependent.

Broadly, we wish to predict what kinds of galaxies the JWST will observe and their distributions of stellar mass and SFRs of those galaxies from $z = 5$ to $z = 10$. The main question is whether those observations would be enough to establish the existence of a SFS out to $z = 10$ and the parameters describing it. We choose to make predictions on the galaxies that will be observed in the $\sim 2\mu\text{m}$, F200W filter with NIRCam on the JWST. As the F200W is the most sensitive imaging filter it will be an important component in the construction of high redshift sources (Rigby et al. 2022).

This paper is laid out as follows. In Section 2 we describe the main differences between FLARES and SHARK, and we make note of the cosmological parameters and initial mass functions (IMFs) that are used in the two simulations. In Section 3 we calculate predictions of stellar mass functions (SMF) and SFRs. In Section 4 we calculate predictions on the parameters of the SFS and the stellar mass dependent scatter in the SFS. In Section 5 we predict the cosmic stellar mass and star formation history. In Section 6 we discuss our results, and in Section 7 we present our final conclusions and main points. Unless explicitly specified, we have absorbed cosmological dependencies in our results. Furthermore, all magnitudes are quoted in AB, unless stated otherwise.

2 SIMULATIONS

We introduce the two galaxy formation simulations used in this work: FLARES, a hydrodynamical zoom simulation (Section 2.1), and SHARK, a semi-analytic model of galaxy formation (Section 2.2). We explore differences between the dust and stellar population synthesis (SPS) models between the two simulations in Section 2.3.

2.1 FLARES

FLARES (First Light And Epoch of Reionisation) was introduced in Lovell et al. (2021) and Vijayan et al. (2021). Below we summarise the baryon model (§ 2.1.1) and the way the spectral energy distribution (SED) of galaxies is computed in FLARES (§ 2.1.2).

2.1.1 Modelling and resimulation method

FLARES is a series of cosmological hydrodynamic zoom simulations built on the EAGLE galaxy formation model (Schaye et al. 2015; Crain et al. 2015) and therefore utilises the modelling techniques and sub-grid recipes used in EAGLE. EAGLE is a suite of smoothed-particle-hydrodynamics simulations run on the P-GADGET3 N-body Tree-PM code that was last described in Springel et al. (2005) and uses the ANARCHY (see Schaller et al. (2015) for details) code to solve the coupled equations of hydrodynamics. EAGLE includes a swathe of sub-grid recipes including radiative cooling and photo-heating, star formation, stellar evolution and chemical enrichment, black hole growth and feedback from active galactic nuclei (AGN) and massive stars (see Schaye et al. (2015); Crain et al. (2015) for further details on the sub-grid models). EAGLE was tuned to the $z \sim 0$ galaxy SMF, stellar mass-black hole relation and galaxy sizes, but has also been shown to agree well with observations not explicitly used in the tuning of the sub-grid model free parameters. Relevant for this work, Furlong et al. (2015) showed that the SMF and SFS were reasonably well reproduced in EAGLE up to $z = 4$ and $z = 3$, respectively; Katsianis et al. (2017) showed that the SFR function was reasonably well reproduced up to $z = 4$; and both Katsianis et al.

(2019) and Davies et al. (2019) showed that EAGLE reproduced well the SFS's scatter at $z = 0$.

Unfortunately, the dynamic range of stellar masses and star formation rates in the EAGLE suit is insufficient to probe the most massive and star forming galaxies that exist in the most overdense environments. Being a series of zoom simulations, FLARES is able to sample these rare overdense environments from a larger dark matter-only simulation thereby providing a statistically complete set of environments. FLARES concentrates on redshift snapshots $z = [5, 6, 7, 8, 9, 10]$ and is therefore perfectly suited to provide predictions on what future surveys will be able to conclude about high-redshift galaxies and the epoch of reionisation. Previous studies have sampled the rarest cluster environments. Barnes et al. (2017); Bahé et al. (2017a) for example sampled and resimulated 30 massive galaxy clusters, also with the EAGLE model, with $z = 0$ halo masses $10^{14} \leq M_{200}/M_{\odot} \leq 10^{15.4}$. Attempting to use such a sample to parametrise the universal properties of high redshift galaxies is however troublesome because of the bias toward only massive cluster galaxies that is not representative of the diverse range of galaxy environments present in the Universe. A prediction of the properties of all galaxies in the early Universe thus requires an unbiased set of simulated galaxies existing in a range of environments and possessing a range of masses. FLARES has generated a set of galaxies that are representative of the entire Universe by sampling from a range of 40 overdensities and applying statistical weights to each region (Lovell et al. 2021). The zoom regions are selected from the 3.2^3Gpc^3 dark matter-only EAGLE box, which is also used in Barnes et al. (2017). 40 spherical zoom regions with radius $14h^{-1} \text{cMpc}$ are resimulated down to $z = 4.67$ at the same resolution as the fiducial EAGLE simulation and with identical physics and parameters. The benefit of this is a sample representative of the early universe with sufficient number statistics on the most massive, clustered galaxies, but unbiased to those.

The range of overdensities of the large dark-matter only box is partitioned into 50 bins of equal width in $\log_{10}(1 + \delta)$, and the i^{th} bin is assigned a statistical weight, $w_{\text{true},i}$, according to the proportion of resimulated overdensities that exist in the bin against the total quantity of overdensities in the box, such that $\sum_i w_{\text{true},i} = 1$. Each of the resimulated regions are also distributed over the bin size, and are assigned weights, $w_{i,j}$, according to the proportion of resimulated overdensities in the bin against the total quantity of the 40 resimulated overdensities, once again so that $\sum_i w_{ij} = 1$. The weight per bin associated with the resimulated regions is then $w_{\text{sample},i} = \sum_j w_{ij}$. Each density bin is then weighted by $r_i = w_{\text{true},i}/w_{\text{sample},i}$. In order for each resimulation region, j , to be statistically representative of the cosmic distribution, it is weighted by $f_j = \sum_i r_i w_{i,j}$ with $\sum_j f_j = 1$. The weights do not change with redshift since the relative ordering of the overdensities is expected to be invariant through $z = 10 \rightarrow 5$ as even the greatest overdensities would be a result of only mildly non-linear evolution.

Structures are found in FLARES first from a Friends-Of-Friends finder (Davis et al. 1985), and bound substructure is further identified with the SUBFIND algorithm (Springel et al. 2001).

The dark matter particle mass resolution of the large 3.2^3Gpc^3 dark matter-only box is $m_{\text{DM}} = 8.01 \times 10^{10} M_{\odot}$ and the gravitational softening length is 59cpc (note this is the same simulation used in Barnes et al. 2017; Bahé et al. 2017b to select the regions to resimulate). The gas particle mass and dark matter particle mass in the fiducial EAGLE simulation, and therefore FLARES, is $m_{\text{gas}} = 1.8 \times 10^6 M_{\odot}$ and $m_{\text{DM}} = 9.7 \times 10^6 M_{\odot}$ respectively; and the softening length is $\epsilon = 2.66 \text{cpc}$. EAGLE, and by extension FLARES, use the Planck Collaboration et al. (2014) Λ cold dark mat-

ter (Λ CDM) cosmology with $H_0 = h \times 100 \text{Mpc kms}^{-1}$, $h = 0.6777$; $\Omega_{\text{m}} = 0.307$ and $\Omega_{\Lambda} = 0.693$. FLARES adopts a universal Chabrier initial mass function (Chabrier 2003).

2.1.2 Dust attenuation calculation in FLARES

The light emitted by stars is attenuated by a two-phase dust medium, the birth clouds, which attenuate young stars, and the diffuse dust in the interstellar medium, which attenuates both young and older stars. Dust attenuation can be quantified by an examination of the optical depth in the V-band (550nm), τ_{V} , and seeing how this is affected by the dust. The emission from each simulated galaxy is computed using version 2.2.1 of the Binary Population and Spectral Synthesis (BPASS) stellar population synthesis (SPS) code (Eldridge et al. 2017; Stanway & Eldridge 2018). Stellar clusters form below sub-kpc scales meaning that dust attenuation from the birth clouds must be calculated using a sub-grid recipe, as:

$$\tau_{BC,V} = \begin{cases} \kappa_{BC} \times (Z_{\star}/0.01) & t \leq 10^7 \text{yr}, \\ 0 & t > 10^7 \text{yr}, \end{cases} \quad (1)$$

where κ_{BC} is a normalisation that encodes information about the physical properties of the dust grains and the dust-to-metal ratio of the birth clouds, and Z_{\star} is the metallicity of the star particle. The optical depth is sensitive to the age of the stellar populations and the piecewise function is obtained from Charlot & Fall (2000) who find that birth clouds disperse by 10^7 years, beyond which there are few attenuating particles around the stellar cluster and hence the optical depth of the birth cloud tends to zero.

In the case of the diffuse dust component, the metal content of the ISM is used as a proxy of dust content (Vijayan et al. 2021). The metal content of the interstellar medium is directly determined from the SPH particles.

The equation to calculate the V-band optical depth is

$$\tau_{ISM,V} = \text{DTM} \kappa_{\text{ISM}} \Sigma(x, y) \quad (2)$$

where DTM is the dust-to-metal mass ratio of the galaxy, κ_{ISM} is a normalisation that encodes information about the physical properties of the dust grains and $\Sigma(x, y)$ is the metal column density integrated over a line of sight. The DTM ratio adopted in FLARES is a fitting function Vijayan et al. (2019, Equation 15) that connects the dust-to-metal mass ratio to the age and metallicity of the galaxy. This function fits the relation between the three latter quantities in the semi-analytic model of galaxy formation L-GALAXIES, and specifically the version introduced in Vijayan et al. (2019) which includes a model for dust formation, growth and destruction. $\Sigma(x, y)$ is evaluated by integrating the density field of SPH particles and linking this to the metallicity and mass of each particle along the line of sight. The viewing angle is fixed such that the line of sight is along the z -axis of the simulation. This prescription yields a sufficient calculation of interstellar medium attenuation without having to simulate the distinct geometry and properties of the dust.

Attenuation from both physical components, described with Equation (1) and Equation (2), is combined with a general wavelength dependence as

$$\tau_{\lambda} = (\tau_{\text{ISM}} + \tau_{\text{BC}}) \times (\lambda/550 \text{nm})^{-1}. \quad (3)$$

At all redshifts, $\kappa_{BC} = 1$ and $\kappa_{\text{ISM}} = 0.0795$. FLARES does not include any redshift evolution of the dust grain sizes, masses or composition.

2.2 SHARK

The second simulation used in this work is the semi-analytic model of galaxy formation SHARK, first introduced in [Lagos et al. \(2018\)](#).

2.2.1 N-body skeleton and semi-analytic method

The cosmic structure in SHARK is provided by the N-body dark matter only simulation Synthetic Universe For Surveys: SURFS ([Elahi et al. 2018](#)). SURFS was designed to provide theoretical test beds to compliment ongoing and upcoming galaxy surveys. SURFS was run using a memory-lean version of the GADGET-2 code ([Springel 2005](#)), producing a variety of box sizes between $40h^{-1}\text{cMpc}$ and $210h^{-1}\text{cMpc}$, each including between 512^3 to 1563^3 dark matter particles. Different simulation boxes also cover a variety of particle masses and softening lengths. The SURFS box that underpins the SHARK simulation used in this work is the L210N1563 simulation that has box size $L_{\text{box}} = 210h^{-1}\text{cMpc}$, number of dark matter particles $N_p = 1563^3$, dark matter particle mass $m_{\text{DM}} = 2.21 \times 10^8 h^{-1} M_{\odot}$ and softening length $\epsilon = 4.5h^{-1}\text{ckpc}$. In total, 200 snapshots spaced in logarithmic intervals of growth factor from redshift $z = 24$ to $z = 0$ were produced using the [Planck Collaboration et al. \(2016\)](#) ΛCDM cosmology with cosmological parameters: $H_0 = h \times 100\text{Mpc kms}^{-1}$, $h = 0.6751$; $\Omega_m = 0.3121$, $\Omega_b = 0.0491$ and $\Omega_{\Lambda} = 0.6879$ being the Hubble’s constant, matter density, baryon density and Λ density respectively.

Dark matter halos and their substructure are identified using the halo finding code, VELOCIRAPTOR ([Cañas et al. 2019](#); [Elahi et al. 2019a](#)), and merger trees of dark matter halos are constructed using the halo merger tree builder, TreeFrog ([Elahi et al. 2019b](#)).

The dark matter halo catalogues from SURFS provide the static skeletons that SHARK uses to simulate galaxies. Since links between halo descendants are found for only up to 4 snapshots into the future, it can be the case that discontinuities exist in the merger trees across snapshots. To smooth over these discontinuities and enforce continuity over the equations of galaxy formation, SHARK places subhalos between the snapshots of the current subhalo and its descendent, if snapshots were skipped by TreeFrog. The dark matter reservoir in which galaxies are embedded are assumed to have an NFW profile ([Navarro et al. 1997](#)).

Galaxies are evolved by first finding the halos that first appear in the snapshot and do not have a progenitor. The most massive subhalo of these first generation halos are assigned a gas supply of mass

$$M_{\text{gas}} = \Omega_b / \Omega_m \times M_{\text{halo}}, \quad (4)$$

and these artificial galaxies are then evolved forward in time. The differential equations that determine the mean mass and metallicity of the baryonic components that are simulated in SHARK are given by Equations 49-58 in [Lagos et al. \(2018\)](#). In SHARK, the physical modelling includes: baryonic matter accretion onto halos, radiative gas cooling, star formation in discs and bulges, stellar feedback, reincorporation of ejected gas, chemical enrichment, galaxy mergers, disc instabilities, photoionisation feedback, black hole growth and AGN feedback and environmental effects. As SHARK lacks the ability to model complex morphologies of galaxies, the basic morphological description that is used is a bulge-disc distinction. This distinction is important because the assembly of stellar mass, and subsequent chemical enrichment, in either the disc or the bulge is not necessarily identical. This distinction is reflected in the star formation law that is a function of the molecular-to-atomic gas fraction, surface density of gas and pressure in either the disc or the bulge, depending on where the star formation is occurring. In addition, it is assumed that star

formation proceeding in the bulge in the form of starbursts converts the molecular gas into stars more efficiently (by a factor of 10) than star formation occurring in the disc.

For extended details on this modelling, the reader is referred to [Lagos et al. \(2018\)](#). SHARK adopts a universal Chabrier IMF ([Chabrier 2003](#)).

2.2.2 Dust attenuation calculation in SHARK

The work horse behind the lighting of SHARK galaxies is PROSPECT ([Robotham et al. 2020](#)), a multiwavelength spectral energy distribution package capable of generating and fitting spectral energy distributions under the consideration of many different astrophysical mechanisms. PROSPECT by default utilises the SPS libraries of [Bruzual & Charlot \(2003\)](#), though the highly flexible nature of PROSPECT allows for the use of many different SPS libraries (such as e-MILES, [Vazdekis et al. 2016](#), and BPASS, [Eldridge et al. 2017](#)). Dust attenuation is described using the model of [Charlot & Fall \(2000\)](#). Star formation and metallicity histories from SHARK galaxies are fed to PROSPECT with sensible assumptions about how dust attenuates galaxy emission and how energy is then reradiated in the infrared. Much like FLARES, the attenuation is multicomponent in nature being related to the optical depth of both birth clouds and the interstellar medium.

There are four distinct methods of dust attenuation that are included in SHARK, and the reader is referred to [Lagos et al. \(2019\)](#) for further details on all of them. Here we only concentrate on methods 3 and 4 as referred to in [Lagos et al. \(2019\)](#), and we briefly outline them below.

The optical depth of the diffuse ISM is modelled as

$$\tau_{\text{ISM}} = \tau_{\text{ISM},V} \times (\lambda/550\text{nm})^{\eta_{\text{ISM}}}, \quad (5)$$

[Trayford et al. \(2020\)](#) use the radiative transfer code SKIRT ([Camps & Baes 2015](#)) to derive scaling relations between $\tau_{\text{ISM},V}$, η_{ISM} and the surface density of dust Σ_{dust} for galaxies between $z = 0 \rightarrow 2$ in the EAGLE simulation, finding the relationships to be mostly independent of redshift. In SHARK the dust surface density is computed for each galactic component (disc and bulge), and the attenuation parameters of Equation (5) are determined by sampling the scaling relations of [Trayford et al. \(2020\)](#). Note that these parameters are found independently for the bulge and disc.

The optical depth due to the birth cloud is

$$\tau_{\text{BC}} = \tau_{\text{ISM}} + \tau_{\text{BC},V} \times (\lambda/550\text{nm})^{\eta_{\text{BC}}}, \quad (6)$$

The V-band optical depth of the birth cloud is derived from the following equation:

$$\tau_{\text{BC},V} = \tau_{\text{BC},0} \frac{\text{DTM} Z_{\text{gas}} \Sigma_{\text{gas,cl}}}{\text{DTM}_{\text{MW}} Z_{\odot} \Sigma_{\text{MW,cl}}} \quad (7)$$

$\tau_{\text{BC},0} = 1$, DTM is the dust-to-metal ratio, Z_{gas} is the gas metallicity, $\Sigma_{\text{gas,cl}}$ is the surface density of gas, $\text{DTM}_{\text{MW}} = 0.33$ is the dust-to-metal ratio of the Milky Way, $Z_{\odot} = 0.0189$ is the solar metallicity and $\Sigma_{\text{MW,cl}} = 85 M_{\odot} \text{pc}^{-2}$ is the typical surface density of molecular clouds in the Milky Way ([Krumholz et al. 2009](#)). The value of η_{BC} is taken to be the default for the [Charlot & Fall \(2000\)](#) attenuation model: $\eta_{\text{BC}} = -0.7$.

The dust masses, which are used to compute Σ_{dust} , are by default determined from the metallicity of the gas in the galaxy according to the best fitting $M_{\text{dust}}/M_Z - Z_{\text{gas}}$ relation computed by [Rémy-Ruyer et al. \(2014\)](#). An alternative method for calculating dust masses uses a steeper fit to the $M_{\text{dust}}/M_Z - Z_{\text{gas}}$ within the errors of the best-fitting relation, which is more consistent with the more recent data

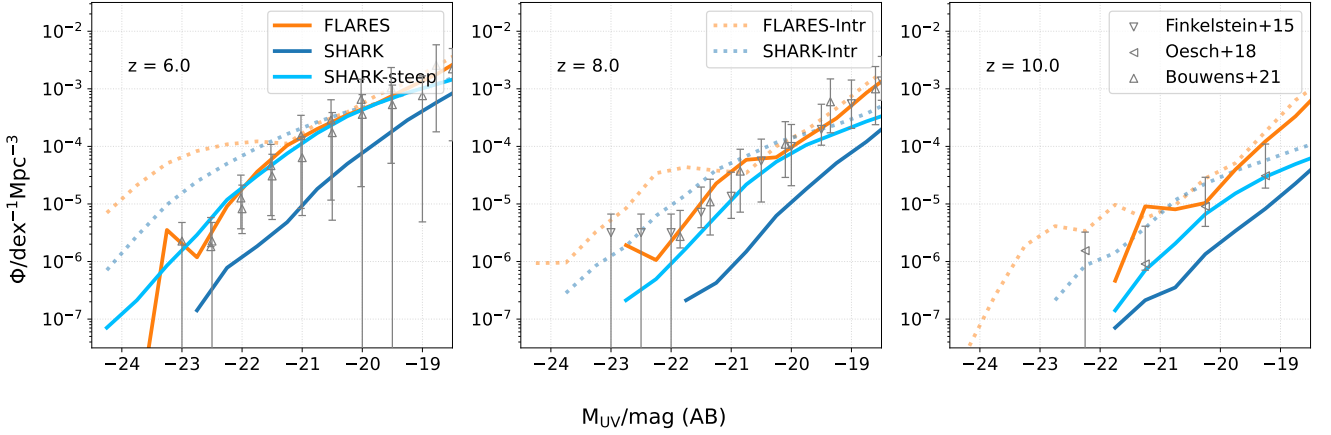


Figure 1. Obscured rest-frame FUV LFs for FLARES (orange), SHARK-default (blue) and SHARK-steep (light blue) at redshifts $z = 6, 8, 10$, as labelled. The dotted lines show the intrinsic LFs for FLARES and SHARK. Grey symbols with error bars show observational constraints of the obscured rest-frame FUV LFs from Finkelstein et al. (2015); Oesch et al. (2018); Bouwens et al. (2021). It is apparent that FLARES and SHARK-steep offer the best fits to the observations, while SHARK-default predicts number densities that are too low.

of De Vis et al. (2019). SHARK uses these as the dust-to-metal ratio. The surface density of the dust is computed for discs and bulges separately according to the following equations;

$$\Sigma_{\text{dust,disc}} = \frac{0.5 M_{\text{dust,disc}}}{\pi r_{50,\text{disc}}^2 l_{50}}, \quad (8)$$

where $M_{\text{dust,disc}}$ is the dust mass in the disc, $r_{50,\text{disc}}$ is the half-gas mass radius of the disc and $l_{50} = \sin(i) \times (r_{50,\text{disc}} - r_{50,\text{disc}}/7.3) + r_{50,\text{disc}}/7.3$ is the projected minor axis with inclination i . The factor 7.3 originates from the average ratio between the scale height and scale length observed in local galaxy discs (Kregel et al. 2002), and the inclination is determined from the angular momentum vector of the host sub halo or chosen randomly for orphan galaxies. For bulges,

$$\Sigma_{\text{dust,bulge}} = \frac{0.5 M_{\text{dust,bulge}}}{\pi r_{50,\text{bulge}}^2}, \quad (9)$$

where $M_{\text{dust,bulge}}$ is the dust mass of the bulge and $r_{50,\text{bulge}}$ is the half-gas mass radius of the bulge. Bulges are considered to be spherically symmetric so the inclination is unimportant.

The two models are thus referred to as

- EAGLE- τ RR14, which is the default for SHARK and uses the EAGLE parametrisation of the Charlot & Fall (2000) model presented in Trayford et al. (2020) and the best-fitting relation of the $M_{\text{dust}}/M_Z - Z_{\text{gas}}$ from Rémy-Ruyer et al. (2014).
- EAGLE- τ RR14-steep that is the same as above but uses a steeper relation for the $M_{\text{dust}}/M_Z - Z_{\text{gas}}$. This indicates that this model will have lower dust masses for fixed metallicities than the previous model.

We choose to concentrate on only two of the possible four dust models included in SHARK here for the purpose of demonstrating the varying effects of dust models upon a single simulation.

2.3 SPS and Dust Models: comparing FLARES and SHARK

We investigate how different parameters used in the generation of the artificial spectral energy distributions affect the emission of our

simulated galaxies. Later we use synthetic photometry to apply magnitude cuts in galaxies to isolate those that would be considered JWST detected.

Figure 1 shows the obscured rest-frame far ultraviolet (FUV, $\sim 1500\text{\AA}$) LFs at $z = 6, 8, 10$. We show the effect of using both the default and steep dust models in SHARK as described in Section 2. We do not have the flexibility to adopt different methods for determining the parameters in Equations (1) and (2) for FLARES in an efficient way as the use of a range of possible recipes that treat the dust is computationally expensive to run. We also do not perform any stellar mass cut in these plots. Observational constraints of the rest-frame UV LFs at these redshifts from Finkelstein et al. (2015); Oesch et al. (2018); Bouwens et al. (2021) are shown. These use a combination of optical and near infrared images from the Hubble Space Telescope. We also show the unobscured LFs of each simulation for reference. The unobscured LFs are similar to the obscured ones at the faint end but diverge at the bright end, where there is significant difference between the intrinsic and obscured brightness per unit volume, showing that the effect of dust upon the FUV LF is significant, even at $z = 10$ in both FLARES and SHARK. Because of the highly flexible nature of SHARK and PROSPECT, we are able to investigate the effect of using the BPASS (Eldridge et al. 2017; Stanway & Eldridge 2018, version 2.2.1) and BC03 (Bruzual & Charlot 2003) SPS libraries on the intrinsic rest-frame UV and optical emission, and we found that the differences between using these two libraries is minimal. Therefore, although FLARES uses BPASS, we continue to use the default BC03 library with SHARK for consistency with previous SHARK papers.

The default SHARK dust model causes a greater deficit in the FUV brightness than the steep model over nearly all magnitudes at each redshift, as expected from the higher dust mass at fixed metallicity in this model than in the steep model. While both simulations agree reasonably well with the observational results, such as the UV-FIR emission of galaxies (eg. Lagos et al. 2018, 2019; Vijayan et al. 2021, 2022), it is important to highlight the large uncertainties that characterise current observational measurements. Due to the SHARK-steep dust model matching these observations far better than the default model, we will use the steep dust model wherever we make use of SHARK photometry within the subsequent sections. Lagos et al. (2019) showed that the normalisation of the $z = 0$ FUV LF predicted

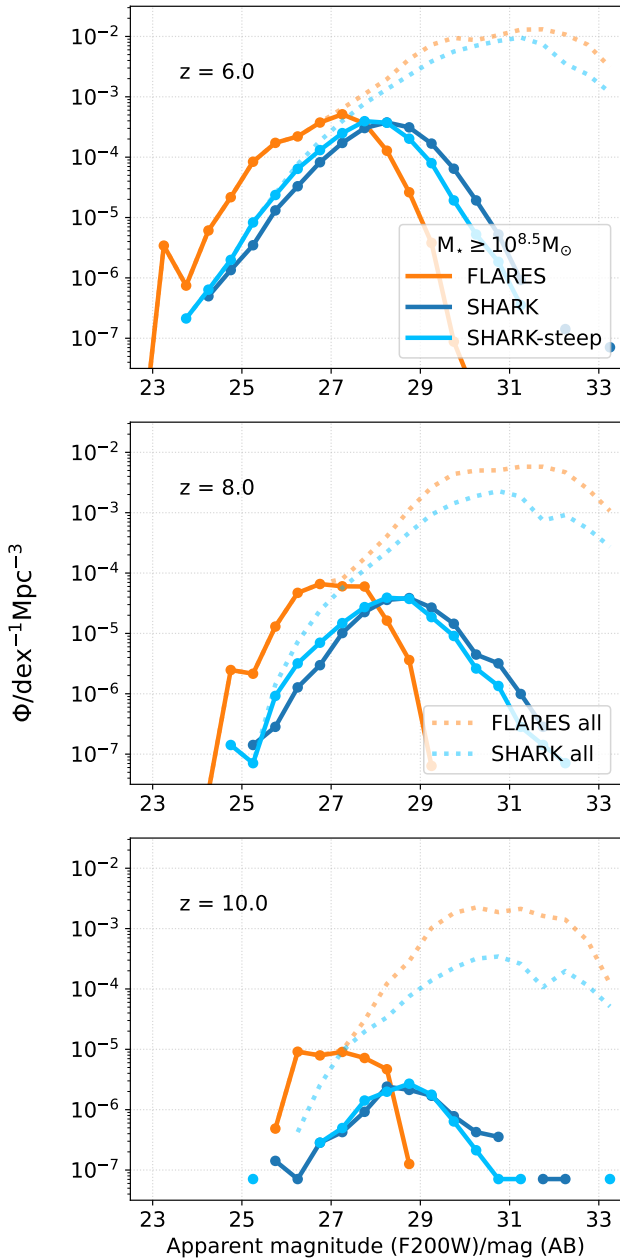


Figure 2. The JWST NIRCAM F200W apparent magnitude volume weighted distribution in FLARES (orange), SHARK-default (blue) and SHARK-steep (light blue) at redshifts $z = 6, 8, 10$. We have performed a stellar mass cut of $M_{\star} \geq 10^{8.5} M_{\odot}$. The faint dotted lines show the LFs for all galaxies in FLARES and SHARK-steep.

by steep SHARK model was slightly higher around the break, L^* , than the default model by a fraction of a dex. The fact that the steep model provides a better fit to the observed UV LFs at $z > 6$ means that either we require a redshift dependent dust-to-metal ratio relation or a chemical evolution model that enriches galaxies more slowly than the current instantaneous recycling model in SHARK. We come back to this discussion later in the context of the predicted cosmic stellar mass and SFR history.

The distribution of galaxies that will be recoverable with the JWST, using NIRCAM and the F200W filter for example, depends on the

fraction of $\lambda \lesssim 0.5 \mu\text{m}$ photons that escape from the galaxy at $z \gtrsim 5$. Figure 2 shows the apparent magnitude distribution per unit volume in the F200W band for FLARES and SHARK galaxies. As with the FUV LFs, both simulations predict similar shapes to the F200W distributions over the breadth of the magnitude domain and throughout redshift. The SHARK steep model predicts more bright galaxies than the default model, and the cause of this difference is the same as it is for the UV LFs in Figure 1. These differences are, however, lesser than those seen in Figure 1 as the rest wavelength traced by the JWST is less affected by dust than that traced by the Hubble Space Telescope, for example, at $z \gtrsim 5$. Also note that both simulations have a peak at around ~ 30 mag. This peak is driven by resolution effects becoming significant at higher magnitudes, as galaxies with stellar masses $\lesssim 10^{8.5} M_{\odot}$ start to dominate the number density fainter than 30 mag as can be seen from the dotted lines that show the distribution for these galaxies in the simulations. The sensitivity of the JWST in the F200W filter is predicted to be 29 mag, as per the exposure calculator tool¹. Hence, throughout the text we will refer to JWST detected galaxies as those brighter than 29 mag in F200W.

The FUV and Nircam F200W LFs highlight clear differences between FLARES and SHARK. Although variations in the dust model used in simulations can alleviate this tension, fundamental differences in the way that either simulation assembles stellar mass affect the predicted emission of galaxies (eg. Bellstedt et al. 2020; Koushan et al. 2021; Wilkins et al. 2022b). These processes are interconnected as dust tracks metal enrichment that is itself connected to star formation and stellar evolution. As such, it is useful to investigate how each simulation models the distribution of stellar mass and SFR in galaxies out to redshift $z = 10$ and whether the JWST will be able improve our understanding of them.

3 STELLAR MASS FUNCTIONS AND STAR FORMATION RATE FUNCTIONS

Figure 3 shows the stellar mass functions (SMF) and SFR functions (SFRF) for galaxies at redshifts $z = 6, 8, 10$ in both FLARES and SHARK. Note that here we present the predictions assuming no errors in stellar mass or SFRs. It is common, however, for predictions to be presented assuming random errors for stellar mass and SFR, which due to the Eddington bias, tend to shift the high-mass end towards higher stellar masses or SFRs (e.g. Lagos et al. 2018). We use the instantaneous SFRs of the galaxies in the results presented for both simulations. For FLARES galaxies we follow Lovell et al. (2021) and define the stellar mass as the total mass of star particles within a 30 kpc aperture centred on the potential minimum of the subhalo, as such the SFR of FLARES galaxies is taken to be within the same aperture. We use these definitions throughout this work.

An important effect for which we must account that motivates our particular selection is the stellar mass resolution of simulated galaxies. Schaye et al. (2015) and Furlong et al. (2015) suggest that galaxies are sufficiently well sampled provided that they consist of at least 100 star particles, which for the star mass resolution of EAGLE and therefore FLARES, results in a mass resolution of $M_{\star}^{\text{lim}} \approx 10^{8.2577} M_{\odot}$ in the simulation. In a similar fashion, reasonably sampled dark matter halos include 100 dark matter particles in the SURFs simulations (Elahi et al. 2018) that precipitates into a galaxy stellar mass resolution of $M_{\star}^{\text{lim}} \approx 10^8 M_{\odot}$ when considering the gas seeding and star formation recipes in SHARK (Lagos et al. 2018; Elahi et al. 2018).

¹ <https://jwst.etc.stsci.edu>

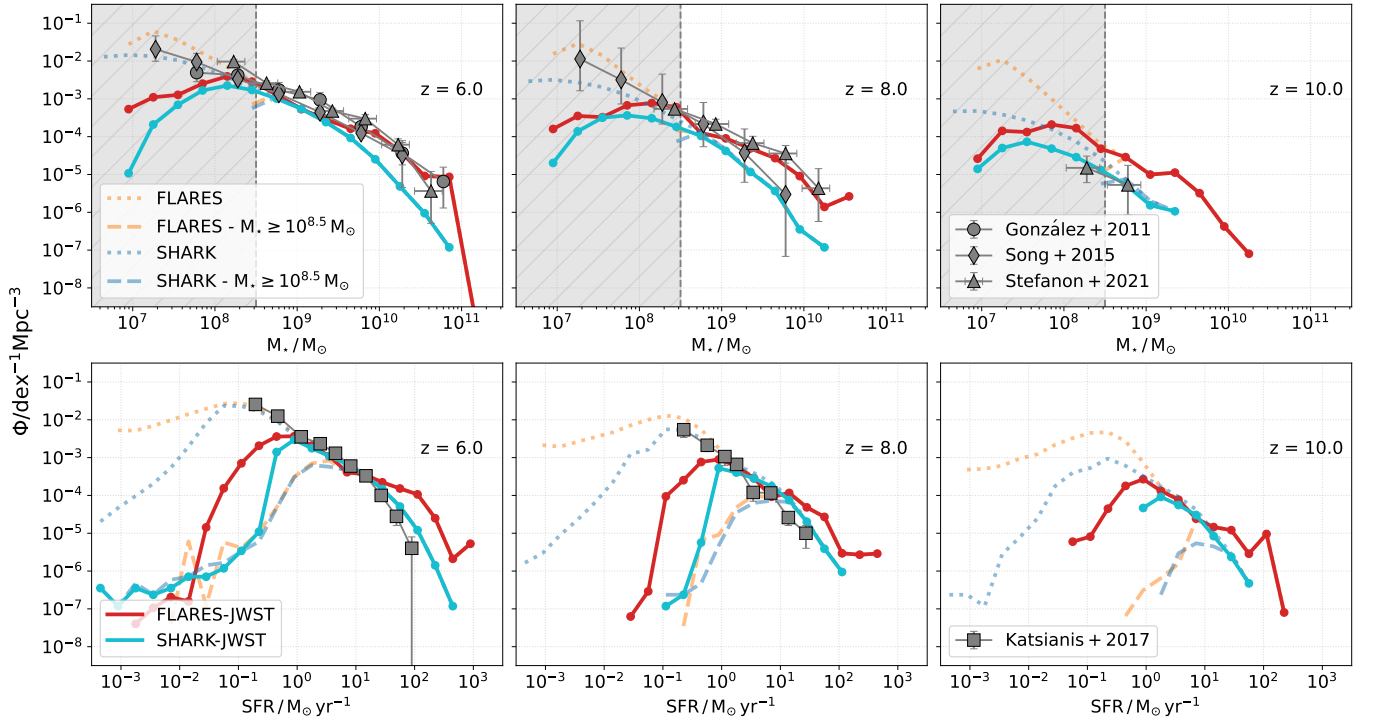


Figure 3. SMFs (top) and SFRFs (bottom) at redshifts $z = 6, 8, 10$. The light coloured, dotted lines show these quantities for the total population of galaxies in the FLARES (orange) and SHARK (blue). The light coloured dashed lines show these quantities for the galaxies with stellar masses above $10^{8.5}M_{\odot}$ in FLARES (orange) and SHARK (blue). The solid lines show these quantities for the JWST detected populations in FLARES (red) and SHARK (cyan). Points with error bars show observational constraints of the SMF from [González et al. \(2011\)](#); [Song et al. \(2016\)](#); [Stefanon et al. \(2021\)](#) and SFRF from [Katsianis et al. \(2017\)](#).

We thus show the distributions of galaxies with $M_{\star} \geq 10^{8.5}M_{\odot}$ with the dashed, coloured lines.

Below $M_{\star} \sim 10^{8.5}M_{\odot}$, and therefore $SFR \sim 1 M_{\odot}yr^{-1}$, the simulations diverge at all redshifts. This divergence is below the mass resolution of the simulations, so it is likely artificial. At $z = 6$, the simulations agree up to $M_{\star} \sim 10^{10}M_{\odot}$ and $SFR \sim 10^1 \rightarrow 10^2 M_{\odot}yr^{-1}$. For higher stellar masses and SFRs the simulations are in tension, with FLARES predicting an excess in the number densities compared to SHARK. At $z > 6$, the maximum stellar masses and SFRs at which the simulations agree is generally lower than at later redshifts. At $z = 8$ the simulations agree up to $M_{\star} \sim 10^{9.0}M_{\odot}$ and $SFR \sim 10^1 M_{\odot}yr^{-1}$, an order of magnitude lower than the agreement threshold at $z = 6$. By $z = 10$ the stellar mass distributions of the simulations are in tension over all stellar masses, with FLARES predicting a higher number density than SHARK across the whole stellar mass range probed. The extension to higher SFRs and stellar masses in FLARES is due to the larger effective volume of FLARES compared to SHARK. Interestingly, at $z = 10$ the distribution of SFRs agree over a similar SFR range as that at $z = 8$. This indicates that SHARK assembles less stellar mass than FLARES for a SFR in the range where they agree. In section 6 we discuss the causes behind the differences at the high mass end of the SMF between the two simulations. The solid cyan and red lines show the SMF and SFRF for the galaxies that will be detected by JWST at this wavelength. In SHARK and FLARES there is remarkable agreement between the distributions calculated for the total population and the JWST detected population above the resolution limit in the simulations; this means that both simulations predict that the JWST will be able to observe all galaxies of $M_{\star} \geq 10^{8.5}M_{\odot}$ and $SFR \geq 10^0 M_{\odot}yr^{-1}$ out to at least $z = 10$.

The top panels of Figure 3 show observational inferences of the SMF. In particular, the $z = 6$ SMF of ([González et al. 2011](#)) who use a

combination of rest-frame optical, ultraviolet and infrared fluxes obtained from the HST and Spitzer Telescope to derive stellar masses; the SMFs at redshifts $z = 6$ and $z = 8$ from [Song et al. \(2016\)](#) who also use a combination of HST and Spitzer observations, which cover a greater area than [González et al. \(2011\)](#); the redshift $z = 6, 8, 10$ SMFs of [Stefanon et al. \(2021\)](#) use a combination of HST and deep IRAC observations. Both simulations generally agree with the available observations within the uncertainties. At the highest redshifts, the observations exhibit large uncertainties meaning that with current observations, the high redshift SMF cannot be well constrained. A good example of the poor constraining power of these observations, is that even though SHARK and FLARES predict different number densities of massive galaxies at $z = 8$, different sets of observations appear to prefer one or the other model. Critically, these observations at these extreme redshifts are almost entirely derived from short wavelength observations that are sensitive to the methods that are used to correct for dust attenuation. Additionally, some estimates require near infrared measurements to make use of the full galaxy SED to determine the stellar mass for the highest redshift objects, which is troublesome with previous observatories, such as Spitzer, as a result of poor NIR sensitivity. This type of systematic uncertainty is not accounted for in the error bars of the observations in Figure 3, nor in the simulations.

A similar story is also true for the observational results shown for the SFRF in the lower panels of Figure 3. We show results from [Katsianis et al. \(2017\)](#) who use the UV LFs of [Bouwens et al. \(2015\)](#) to derive dust-corrected SFRs. [Katsianis et al. \(2017\)](#) use the IRX $-\beta$ of [Meurer et al. \(1999\) and the linear \$\beta - M_{UV}\$ of \[Bouwens et al. \\(2012\\)\]\(#\) to determine the absorption at \$1600\text{\AA}\$, and thus the optical depth, to correct the UV luminosities for dust attenuation following the method of \[Hao et al. \\(2011\\)\]\(#\). It can be seen that there is good](#)

agreement between these results and the predictions of FLARES and SHARK across the range of SFRs probed. It can also be seen that the agreement with these observational results persist for the galaxies below our chosen stellar mass selection. However, this agreement is sensitive to the dust corrections used to derive SFRs. Where possible, we have tried to standardise the cosmologies utilised by the simulations and observations as differences in cosmologies can introduce tensions (Croton 2013); it should however be noted that discrepancies precipitated by different cosmologies are likely dwarfed by differences induced by modelling details, light-to-mass derivations and dust corrections (Speagle et al. 2014).

4 STAR FORMING MAIN SEQUENCE

In this section, we present our predictions on the shape and stellar mass-dependent scatter of the SFS at $z \geq 5$.

4.1 Fitting the SFS

To fit our simulation’s SFS, we follow the same procedures outlined in Thorne et al. (2021) who use a two-component power law. The latter allows to fit a possible turn over in the SFS, which, when present, appears in massive galaxies. Lovell et al. (2021) presented evidence of a turn over in the SFS in FLARES. The functional form of the SFS is thus

$$f(\mathcal{M}) = S_0 - \log_{10} \left[\left(\frac{10^{\mathcal{M}}}{10M_0} \right)^{-\alpha} + \left(\frac{10^{\mathcal{M}}}{10M_0} \right)^{-\beta} \right], \quad (10)$$

where $\mathcal{M} = \log_{10}(M_{\star}/M_{\odot})$, S_0 is the limiting SFR of the function at high stellar mass in units of $\log_{10}(M_{\odot}\text{yr}^{-1})$, M_0 is the stellar mass in units of $\log_{10}(M_{\odot})$ at which the SFS turns over and α and β are the respective low and high stellar mass slopes. Equation (10) from Thorne et al. (2021) is itself an adaptation of the two component model used in Lee et al. (2015) that, instead of assuming that the SFS flattens to a slope of zero at high stellar masses as is the case in Lee et al. (2015), allows for an additional degree of freedom, β , to describe the high stellar mass slope. We use Equation (10) as the foundation of a Bayesian fitting routine. The likelihood function that we maximise is a student-t distribution with a fixed scale of 0.3. We use broad uniform priors on the parameters of the SFS: $S_0 \sim \text{U}(0.01, 4.01)$; $M_0 \sim \text{U}(8.0, 19.0)$; $\alpha \sim \text{U}(0.5, 2.0)$; $\beta \sim \text{U}(0.1, 0.61)$. We are thus hypothesising that the SFS does in fact exist out to $z = 10$ and that its shape is consistent with our function. We estimate the parameters and 1σ uncertainties by performing a Markov-Chain-Monte-Carlo (MCMC) analysis using the Python package EMCEE (Foreman-Mackey et al. 2013). We have elected to not perform any kind of SFR or specific SFR ($\log_{10} \left[\frac{\text{SFR}}{M_{\star}} \text{yr}^{-1} \right]$) selection in defining the SFS here, as is the case in many works that focus on the SFS at lower redshifts in the literature (Davies et al. 2016, 2019, 2022; Katsianis et al. 2019). Our choice is motivated by the fact that we do not expect a significantly quenched and off-SFS galaxy population contained in our high redshift sample. We note, however, that there are passive galaxies in FLARES up to $z \sim 8$ though they constitute $< 3\%$ of the total population (Lovell et al. in prep).

Figure 4 shows the 5th – 95th percentiles and medians between redshifts $z = 5 \rightarrow 10$ for the total galaxy populations in both simulations. It is clear that both simulations predict the existence of a tight SFS up to $z = 10$, indicating that the process of self-regulation in galaxy growth is present and efficient in the very early universe.

Despite differences in the stellar mass assembly, the two simulations predict similar SFSs. FLARES exhibits a slightly clearer high stellar mass turn over than SHARK. SHARK exhibits approximately uniform variance in the SFS with stellar mass, whereas FLARES shows more puffed up variance at low and high stellar masses and a minimum in the variance around $\sim 10^9 M_{\odot}$ particularly at $z \lesssim 7$. Note, however, that the increase in the variance at low stellar masses in FLARES happens mostly at the regime where resolution is expected to significantly affect our results. Therefore, the increased scatter is likely dominated by star formation stochasticity and requires higher resolution simulations to probe robustly. We return to the subject of variance about the SFS in Section 4.2. The skew in the SFS at high stellar masses seen in the 5th – 95th percentiles is due to the population of massive galaxies in FLARES undergoing quenching, the cause of which is likely energy injection from their AGN driving a suppression of star formation in massive galaxies.

We also show the fitted relations as solid lines, and it can be seen that the fits agree well with the predicted relations. We only fit galaxies with $M_{\star} \geq 10^{8.5} M_{\odot}$. We do see that the lower stellar mass slope, α , is steeper in FLARES than it is in SHARK at $z \lesssim 7$, which may originate from the highly overdense, starburst galaxy populations that FLARES samples but SHARK does not; this is likely to be strongly related to the enhancement in stellar mass and SFR seen in Figure 3.

Most notably at $z \lesssim 7$ the FLARES fits are able to better capture the full extent of the turn over in the SFS observed in the median trend, with the median showing a slightly higher normalisation around $\sim 10^{9.5} M_{\odot}$ than the fit. This is likely caused by quenching that is driving a cessation of star formation in massive galaxies. The fact that this turn over is not seen in SHARK galaxies below $M_{\star} \sim 10^{10} M_{\odot}$ indicates that massive galaxy quenching occurs earlier in FLARES (Lovell et al. in prep). Above $z \sim 7$ the SFSs of both simulations are remarkably similar, indicating that self-regulation is occurring in a similar fashion between these two simulations.

We have calculated the same parameters of the SFS for the population that will be detected by the JWST in both simulations. We have included Gaussian uncertainties of 0.2 dex and 0.4 dex on the stellar masses and SFRs of the JWST populations respectively to account for potential uncertainties in deriving those quantities from actual observations. We investigate the effect of uncertainties more closely in Appendix A. Remarkably, the JWST population is very closely congruent with the total population in the simulations over the entire SFR – M_{\star} plane at all redshifts shown in Figure 4. This indicates that planned JWST observations are deep enough to recover the SFS.

Figure 5 shows the redshift evolution of the parameters of the SFS for SHARK and FLARES, for both the total and JWST galaxy detected populations. Tabular data of these fits is recorded in Table 1. The shaded regions and error bars show 1σ uncertainties on the parameter estimates from the MCMC sampling for the total and JWST detected populations respectively. It is interesting that above $z \sim 7$ the simulations predict very similar SFS considering the different modelling processes, and that only $z = 0$ observations were used for the tuning of free parameters. The normalisation evolves similarly in the simulations for all considered redshifts. Below $z \sim 7$, the fitting to the SFS in SHARK indicates a turn over mass that is an order of magnitude higher mass than that in FLARES and a shallower low stellar mass slope. The fitted turn over mass in SHARK is actually higher than the most massive galaxies that the simulations predict, indicating that there is no turn over in the SFS in SHARK at $z \gtrsim 5$. This, in combination with the low stellar mass slope tending to unity, suggests that the SFS in SHARK is better described by a single power law at $z \gtrsim 5$. The main difference between the SFS in the simulations

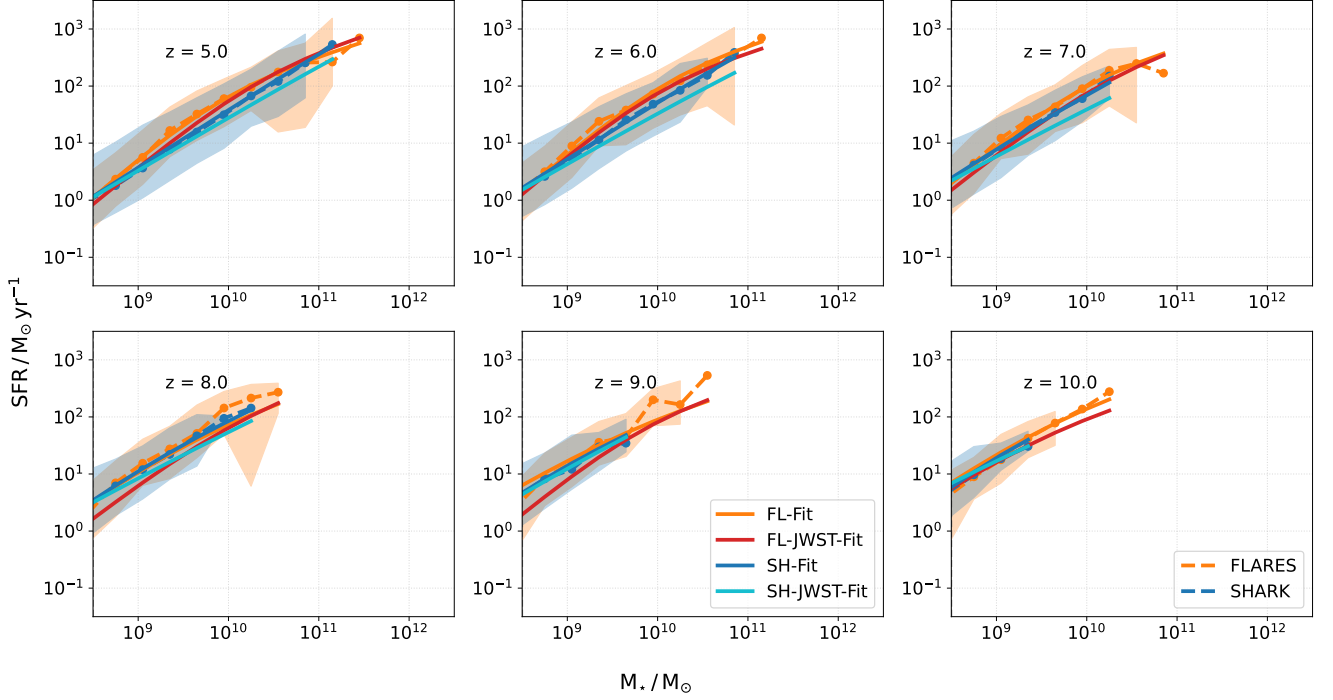


Figure 4. SFR – M_* between redshift $z = 5 \rightarrow 10$ for entire population in FLARES (orange) and SHARK (blue). The dashed lines with markers show the median trend and the coloured shaded regions show the 5th – 95th percentiles. The solid orange and blue lines show the fit to the SFS as per Equation (10) for the population with masses above $10^{8.5}M_\odot$ in FLARES and SHARK respectively. The red and light blue solid lines show the fit for the JWST detected population in FLARES and SHARK respectively. The grey shaded regions highlights the stellar mass resolution limit of $10^{8.5}M_\odot$.

Redshift	S_0	M_0	α	β
FLARES				
5.0	2.40 ± 0.77	10.38 ± 0.75	1.31 ± 0.16	0.46 ± 0.17
6.0	2.18 ± 0.77	10.01 ± 0.77	1.36 ± 0.23	0.44 ± 0.17
7.0	2.32 ± 0.92	10.17 ± 0.97	1.28 ± 0.29	0.47 ± 0.17
8.0	2.18 ± 1.00	10.09 ± 1.14	1.22 ± 0.36	0.47 ± 0.17
9.0	2.11 ± 1.04	9.88 ± 1.23	1.30 ± 0.42	0.42 ± 0.17
10.0	1.98 ± 0.98	9.58 ± 1.33	1.06 ± 0.42	0.40 ± 0.17
FLARES-JWST				
5.0	2.02 ± 0.71	9.90 ± 0.72	1.40 ± 0.21	0.48 ± 0.18
6.0	2.35 ± 0.79	10.11 ± 0.76	1.37 ± 0.23	0.45 ± 0.17
7.0	2.28 ± 0.85	9.98 ± 0.89	1.33 ± 0.29	0.41 ± 0.17
8.0	1.93 ± 0.96	9.69 ± 1.27	1.12 ± 0.40	0.46 ± 0.17
9.0	2.07 ± 0.98	9.73 ± 1.49	0.97 ± 0.41	0.39 ± 0.17
10.0	2.22 ± 0.95	9.69 ± 1.27	1.09 ± 0.43	0.43 ± 0.17
SHARK-JWST				
5.0	3.90 ± 0.32	12.62 ± 0.40	0.93 ± 0.02	0.37 ± 0.24
6.0	3.36 ± 0.88	11.93 ± 1.11	0.92 ± 0.05	0.50 ± 0.21
7.0	2.35 ± 0.94	10.58 ± 1.20	0.92 ± 0.07	0.62 ± 0.17
8.0	2.67 ± 1.03	10.83 ± 1.34	0.90 ± 0.10	0.59 ± 0.17
9.0	2.42 ± 0.91	10.25 ± 1.12	0.98 ± 0.17	0.50 ± 0.18
10.0	2.05 ± 0.97	9.72 ± 1.38	0.89 ± 0.27	0.51 ± 0.17
SHARK				
5.0	3.84 ± 0.19	12.22 ± 0.19	1.01 ± 0.01	0.23 ± 0.14
6.0	3.51 ± 0.94	11.75 ± 1.05	1.01 ± 0.09	0.37 ± 0.21
7.0	2.77 ± 0.85	10.73 ± 0.95	1.05 ± 0.11	0.56 ± 0.19
8.0	1.76 ± 0.73	9.44 ± 0.80	1.18 ± 0.17	0.61 ± 0.16
9.0	1.70 ± 0.84	9.30 ± 0.98	1.14 ± 0.24	0.53 ± 0.17
10.0	1.86 ± 0.82	9.30 ± 0.91	1.24 ± 0.29	0.49 ± 0.17

Table 1. Redshift evolution of the SFS fit parameters and associated $1 - \sigma$ uncertainties as described in Section 4 and shown in Figure 5.

is thus the turn over as a result of quenching, and the redshift at which that quenching becomes prevalent. We elaborate on this in Section 6.

Shown as well are observationally derived estimates on SFS parameters from Thorne et al. (2021) who fit the SFS using the same two-component power law in 20 redshift bins with an equal width of ~ 0.75 Gyrs. SFRs and stellar masses are derived by SED fitting galaxies between $\lambda \sim 0.154 \rightarrow 504 \mu\text{m}$ in the D10-COSMOS field of DEVILS (Davies et al. 2018, 2021). These observations have a coarse temporal resolution at high redshift (with the highest redshift bin being $z = 5 \rightarrow 9$) and a high stellar mass cut of $\gtrsim 10^{10.4}M_\odot$ for $z > 5$ meaning the range of stellar masses probed is small. Despite these caveats, the simulations agree somewhat with the observations. The SFS normalisation is consistent with the simulations at redshift $z \lesssim 9$. The turn over mass is more consistent with SHARK than Flares, with FLARES being lower, however, the turnover mass in SHARK happens above the range of simulated stellar masses and hence is not well constrained. This suggests that the observations favour a single power law SFS at $z \gtrsim 5$, which was a similar conclusion reached in Thorne et al. (2021) who found negligible turn overs beyond $z \sim 2$. To assert that the observations favour one model or the other is disingenuous, however, because the lack of observations here hinder a rigorous exploration of this parameter space. Furthermore, mass completeness limit used in Thorne et al. (2021) is $\gtrsim 10^{10.4}M_\odot$ for $z > 5$ meaning the range of stellar masses probed is small.

We thus predict that the JWST will be able to sufficiently detect all intrinsically bright galaxies and offer for the first time reliable fits to the SFS for the first galaxies to have formed in the Universe. It is encouraging then that we predict that the JWST will be able to recover the SFS for redshifts up to $z = 10$ as these observations will be necessary to decouple slight differences in the simulations. This will elucidate the origins of these kinds of fine distinctions between

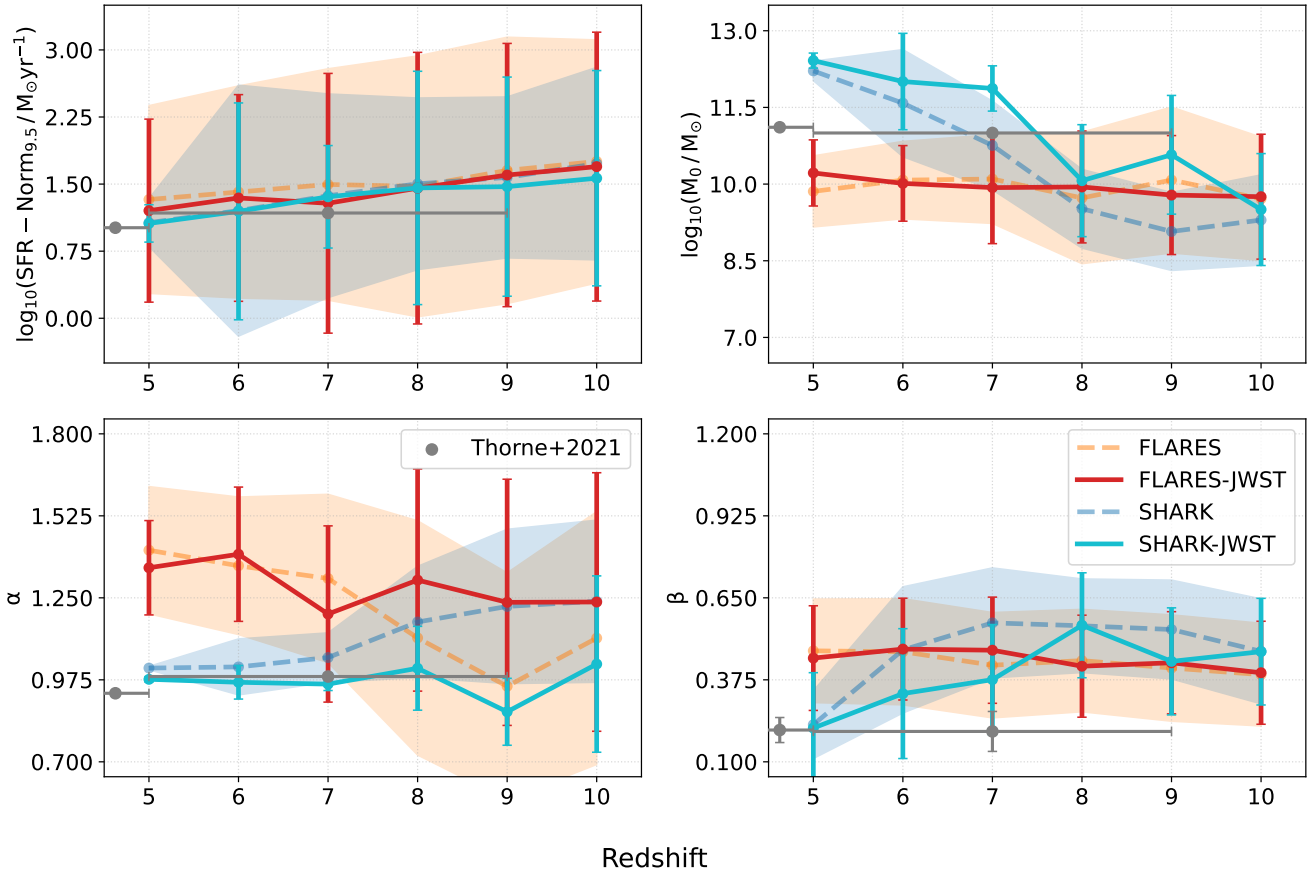


Figure 5. Redshift evolution of the parameters of the SFS as per Equation (10); the normalisation, S_0 , is calculated at $10^{9.5}M_\odot$ instead of the maximum value to which Equation (10) approaches at high stellar masses. The dashed lines with shaded regions show the results and 1σ uncertainties for the total population of galaxies in FLARES (orange) and SHARK (blue). The solid lines with error bars show the results and 1σ uncertainties for the JWST detected galaxies in FLARES (red) and SHARK (cyan). The grey points with error bars show the observational results and uncertainties obtained from Thorne et al. (2021).

the two simulations (and potentially other simulations), which are embodied in galaxy formation theory.

4.2 Stellar mass dependence of the SFS scatter

The usefulness of the SFS is that it encodes information about astrophysical process that may be driving the shape and normalisation. In particular, the stellar mass dependent scatter is an indicator of how effective different feedback mechanisms are in regulating star formation in galaxies. At lower redshifts, $z \lesssim 0.7$, the $\sigma_{\text{SFS}} - M_\star$ has been observed to exhibit a minimum vertex parabolic shape, with its turning point in the neighbourhood of $\sim 10^9 M_\odot$ (Davies et al. 2019, 2022). The minimum point of the stellar mass dependent scatter is interpreted as the galaxy phase at which gas inflow is balanced by both star formation and feedback. Galaxies in this phase experience little variation about the SFS, and so minimal scatter, as gas compaction and subsequent depletion events are highly self regulated for these galaxies (Tacchella et al. 2016).

Figure 6 shows the $\sigma_{\text{SFS}} - M_\star$ for SHARK and FLARES, where σ_{SFS} is the 16th – 84th percentile range. It can be seen that both simulations are fairly consistent about the shape of the relation with stellar mass over most stellar masses and redshifts probed. Below $M_\star = 10^{8.5} M_\odot$ the simulations disagree, with SHARK predicting a decrease in the scatter at $z \gtrsim 9$ and a uniform scatter at $z \lesssim 8$, while FLARES predicts a significant uptick of the scatter at all redshifts. The

decreased scatter in low stellar mass SHARK galaxies at $z \gtrsim 9$ may suggest that they are better self regulated as most are not far off from the SFS. Stochastic star formation then becomes more important at $z \lesssim 8$ to drive up the scatter. Conversely the uptick seen in FLARES throughout all redshifts is likely an effect of stochastic star formation due to the poor resolution at these masses. For both simulations, these effects occur below the stellar mass resolution limit of the simulations however, and so these results cannot be considered robust.

A striking feature of the $\sigma_{\text{SFS}} - M_\star$ is the lack of significant scatter at the massive end, $M_\star \gtrsim 10^{10} M_\odot$, that both simulations predict at redshifts $z = 5 \rightarrow 10$. The likely reason for this is that the massive galaxies at these redshifts in the simulations have not yet had enough time to sufficiently grow their supermassive black holes. AGN feedback is thought to increase the asymmetric variance from the SFS as feedback continuously inhibits star formation and drives massive galaxies below the SFS (Davies et al. 2022). This is consistent with other studies that investigate this effect in simulations (Katsianis et al. 2019). Although there is a general lack of significant scatter at these large stellar masses, with decreasing redshift, FLARES starts to show an increase in $\sigma_{\text{SFS}} - M_\star$ at stellar masses $\gtrsim 10^{10.3} M_\odot$ at $z \sim 5$, which shows the initiation of quenching in these galaxies. This is consistent with lower redshift results from simulations that show that the scatter in the SFS for galaxies $M_\star \gtrsim 10^{10} M_\odot$ increases by 0.05 dex from $z=5$ to $z=0$ (Matthee & Schaye 2019). This is not seen in SHARK. This difference between the simulations together with the JWST-like

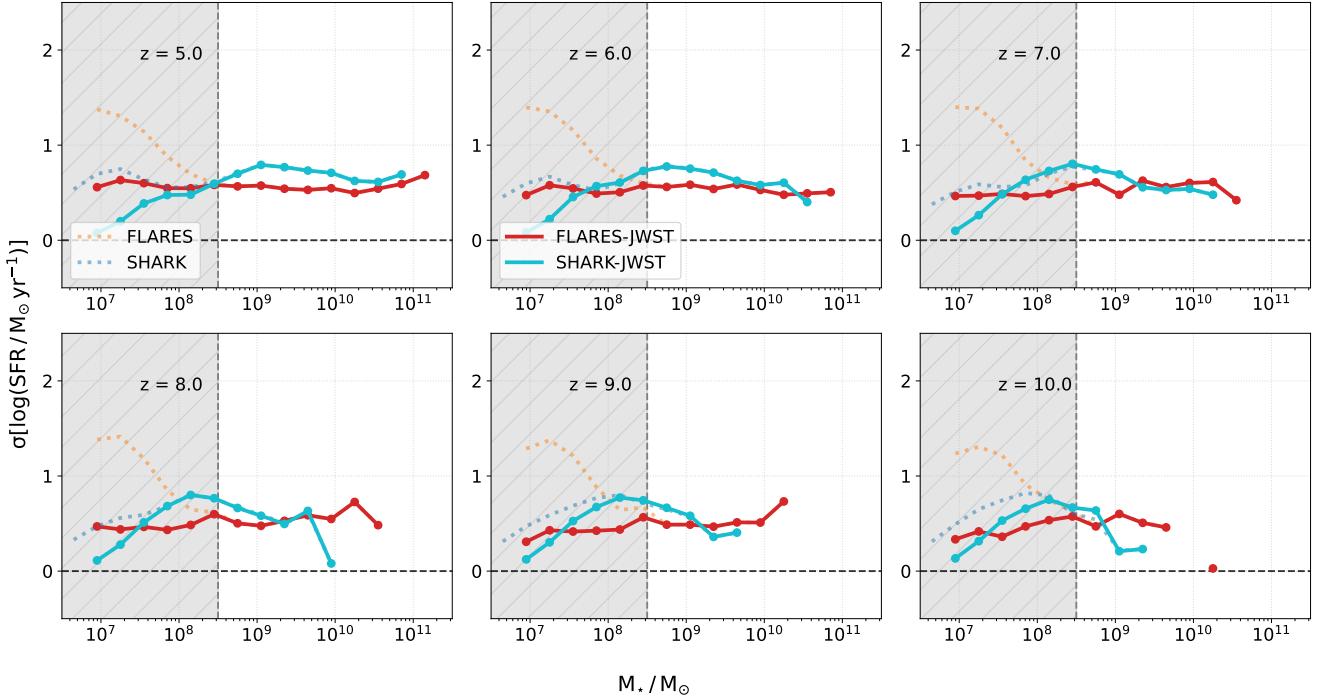


Figure 6. $\sigma_{\text{SFS}} - M_{\star}$ relation for the total galaxy populations in FLARES (orange) and SHARK (blue) at redshifts $z = 5 \rightarrow 10$. Also shown is the same relation but for the JWST detected galaxies in FLARES (red) and SHARK (cyan). The grey shaded regions shows the stellar mass resolution limit, $M_{\star} = 10^{8.5} M_{\odot}$.

samples following the same SFS as all the simulated galaxies, indicates that the JWST will be able to place strong constraints on the onset of quenching in massive galaxies from the characterisation of the SFS at high redshift.

While there is the issue of stellar mass resolution we can conclude that faint dwarf galaxies below the detection sensitivity of the JWST are likely, if not completely, responsible for the disparity between the total and JWST detected populations observed for stellar masses $M_{\star} \lesssim 10^{8.5} M_{\odot}$. JWST will not detect many galaxies with low star formation rates, as was confirmed in Figure 3. This means that the contribution to the scatter about the SFS for low stellar mass objects is biased to those on or above the SFS, which would lead to an underestimation of the scatter. This trend is seen in Figure 6 for both simulations, although again this is the mass range that falls below the resolution of the simulations.

Most importantly, above stellar masses of $10^{8.5} M_{\odot}$ the JWST detected population in each simulation is in agreement with the total population up to the highest stellar masses probed and for all redshifts shown up to $z = 10$. We thus predict that the JWST should be able to sufficiently detect all intrinsically bright galaxies to understand the $\sigma_{\text{SFS}} - M_{\star}$ of the Universe up to redshift $z = 10$.

5 COSMIC STELLAR MASS AND STAR FORMATION RATE HISTORY

Figure 7 shows the cosmic stellar mass and cosmic star formation rate densities (CSMD/CSFRD) as a function of redshift, or cosmic stellar mass/cosmic star formation rate history (CSMH/CSFRH). The dashed lines show the results for all galaxies in the simulations. Both simulations predict consistent shapes of both the CSMH and CSFRH over all redshifts shown. FLARES, however, exhibits a noticeably higher normalisation of both the CSMH and CSFRH compared

to SHARK. FLARES is ~ 4.4 (~ 2.0) times higher in CSMD (CSFRD) than SHARK averaged over redshift, but up to ~ 9.6 (~ 2.9) times larger at $z = 10$. The difference in CSMD becomes systematically smaller with decreasing redshift, with FLARES being ~ 2 times larger than SHARK by $z = 5$. The difference in CSFRD is lowest at $z = 7$ where FLARES is ~ 1.6 times larger than SHARK but becomes ~ 1.9 times larger by $z = 5$. This is potentially a result of the stellar mass and SFR enhancement captured by FLARES as a result of the contribution from overdense environments sampled in FLARES that are not present in SHARK. It can also be seen that the difference in the normalisation between the two simulations is larger in the CSMH than in the CSFRH, which appears to be the result of the different chemical enrichment models used in the simulations. SHARK instantaneously recycles and enriches the interstellar medium with metals following star formation (Lagos et al. 2019), while there is a delay between star formation and enrichment in FLARES to account for the evolution of type Ia and II supernovae and AGB stars (Schaye et al. 2015; Crain et al. 2015). This can explain the larger offset in the CSMH, as more mass is diverted from stars toward metal pollution of the ISM in SHARK than FLARES, particularly at earlier times. The fact that the differences in the CSMH become smaller at later times is the result of the instantaneous recycling approximation becoming a better approximation as the dynamical time of halos becomes longer.

To ensure that resolution effects are not biasing these results, we also examined the CSFRH and CSMH only for galaxies that satisfy $10^{8.5} M_{\odot} < M_{\star} \leq M^{9.0} M_{\odot}$. The reason for this particular selection is to be above the resolution limit but below the stellar mass range where FLARES predicts a much greater number density of stellar mass and SFR compared to SHARK, which would bias our results. We found that the same trends as the total population persist in this case except at $z = 10$ where the difference in normalisation between the CSMD and CSFRD are similar. As such, while chemical enrichment is an important factor in influencing the normalisation of the CSMH and

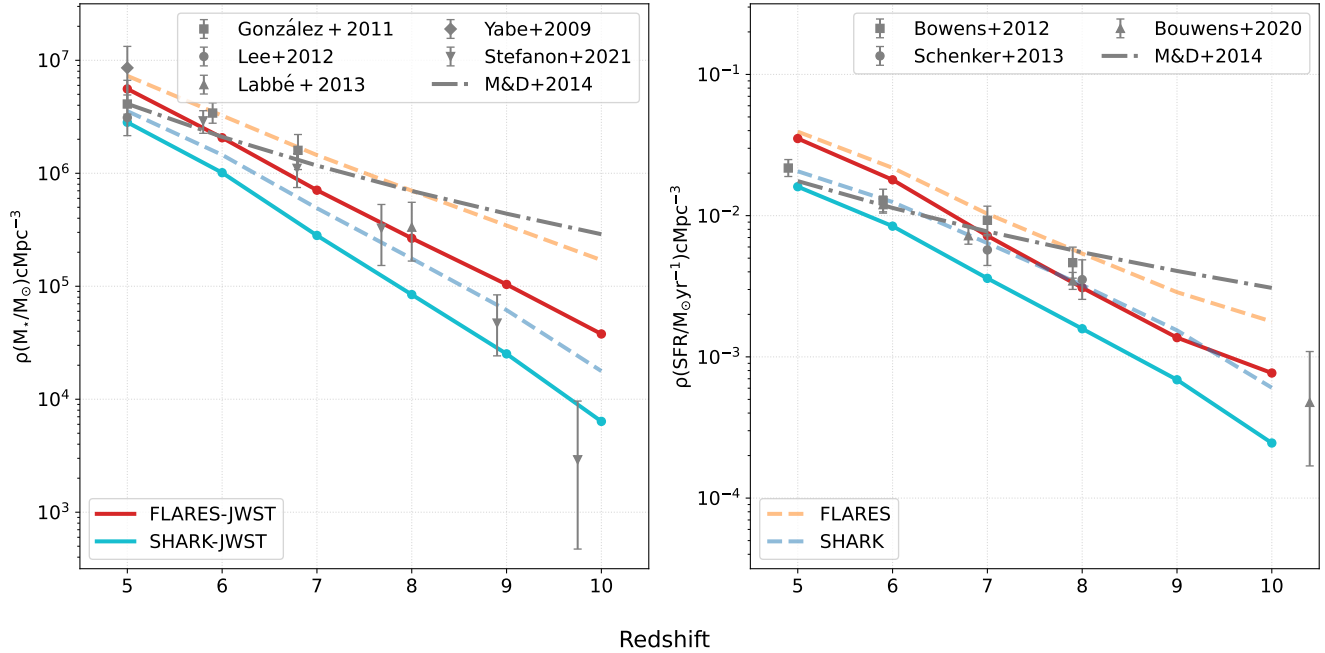


Figure 7. The CSMH (left) and CSFRH (right) at redshifts $z = 5 \rightarrow 10$. The light coloured, dashed lines show these quantities for the entire population of galaxies in FLARES (orange) and SHARK (blue). The solid lines show the results for the population that will be detected by the JWST in FLARES (red) and SHARK (cyan). The dot dashed grey lines show the fits to the CSFRD and CSMD from Madau & Dickinson (2014). Data points with error bars in the left panel show observational results of the CSMH (Yabe et al. 2009; González et al. 2011; Lee et al. 2012; Labbé et al. 2013; Stefanon et al. 2021). In the right panel observational estimates on the CSFRH (Bouwens et al. 2012; Schenker et al. 2013; Bouwens et al. 2020) are shown as data points with error bars.

CSFRH, we cannot rule out different star formation histories also somewhat driving this difference.

We have also included some observational estimates on both the CSMH and CSFRH. The observations on the right panel of Figure 7 show the CSFRH derived by Madau & Dickinson (2014) who curated UV LFs of Bouwens et al. (2012) and Schenker et al. (2013), and then converted them into a CSFRH. The observational data points shown in the left panel are UV-derived estimates of the CSMD (Yabe et al. 2009; González et al. 2011; Lee et al. 2012; Labbé et al. 2013; Stefanon et al. 2021). Where possible, we have standardised the cosmologies and IMFs used for these observational results to be most comparable with our simulations. The observations for both the CSMH and CSFRH are consistent with the shapes of the predicted relations from both simulations up to $z \sim 10$ and $z \sim 8$ for the CSMH and CSFRH respectively. The SHARK predictions of the CSMH and CSFRH are in better agreement with the observations, with FLARES generally predicting a higher normalisation than the observations in both the CSMH and CSFRH over the relevant redshift range. We must again stress, however, that all of these observational estimates are almost entirely from UV sources that are thus affected by the assumptions around dust obscuration corrections.

The solid lines show the cosmic densities for the population that will be detectable with the NIRCam F200W filter of the JWST. We only show the result with a photometric cut, truncating at 29 ABmag, and not a cut in stellar mass. Noticeably, both simulations predict that the JWST detected populations do not account for the entire distribution of stellar mass and SFR in the universe over all these redshifts. Perhaps unsurprisingly, this indicates that there are faint galaxies that fall below the detection sensitivity of the JWST and are not accounted for in the calculation of the CSMH and CSFRH. Fortunately, this is well understood as the Malmquist bias for which

there are numerous correction methods (Weigel et al. 2016). As only the normalisation, and not the shape, of the CSMH and CSFRH for the JWST detected population is different from that of the total population it shows that the JWST should be able to detect every intrinsically bright galaxy out to redshift $z = 10$, just not all galaxies in the universe.

6 DISCUSSION

We have shown that both simulations, FLARES and SHARK, predict that the JWST will be able to observe galaxies with a large enough range of stellar masses and SFRs to allow a thorough study of SFS, including the onset of quenching in massive galaxies, and thus stellar mass assembly during the early Universe. Additionally, we predict that the JWST will be a vital tool to better understand cosmic reionisation as a large census of galaxies that span a high dynamic range of stellar masses and star formation rates will likely encompass ionising sources. Prior observational studies (eg. Thorne et al. 2021) indicate the prevalence of a SFS around $z \sim 5$, and here we show that both the simulations analysed here predict the existence of a SFS up to at least $z = 10$. In this work, we quantified the predicted SFS’s shape and scatter as a function of stellar mass in each simulation. We expect the JWST to be able to test these predictions in the near future. Figure 3 shows that both FLARES and SHARK predict similar intrinsic distributions of stellar mass and SFR which indicates that, although these simulations differ in many details, the sub-grid methods of stellar mass assembly used in each must act similarly. The relative agreement with the existing observations indicate that our understanding of stellar mass assembly must not be so far removed from how the process functions in nature; though, it will be a task

for the JWST to confirm this suspicion with updated, near infrared photometry.

Despite this overall agreement, there are important differences between the two simulations that we discuss below.

6.1 The abundance of massive galaxies

A glaring difference between the simulations is the excess number density of high stellar mass galaxies with high star formation rates at fixed stellar mass in FLARES compared to SHARK. To get to the bottom of this difference, we show in the top panels of Figure 8 the subhalo-stellar mass relation for both FLARES and SHARK at $z = 6, 8, 10$ for central galaxies. We only use centrals in these calculations to simplify the comparison; including satellite galaxies only slightly increases the higher mass, $M_{\star} \gtrsim 10^{10} M_{\odot}$, scatter of these trends. FLARES extends the $M_{\text{subhalo}} - M_{\star}$ 0.2 dex and 1 dex beyond SHARK at $z = 6$ and $z = 10$ respectively. By the fact that the simulations broadly agree on the shape of the relation over all redshifts, it is possible to conclude that the difference in the predicted SMFs is due to FLARES covering a wider dynamic range, extending to rare, large over-densities (i.e. cosmic variance).

Despite the broad agreement between the simulations in the top panel of Figure 8, it is worth highlighting that FLARES predicts slightly more stellar mass for a fixed subhalo mass than SHARK, at $M_{\text{subhalo}} \gtrsim 10^{12} M_{\odot}$ at $z = 6$ and $z = 8$. The lower panels of Figure 8 show the specific SFR as a function of subhalo mass for the simulations at $z = 6, 8, 10$. Especially at $z = 6, 8$, FLARES predicts a higher sSFR than SHARK for $M_{\text{subhalo}} \gtrsim 10^{11} M_{\odot}$, indicating that star formation is more efficient in massive halos in FLARES than in SHARK. Therefore it is likely a combination of both FLARES sampling greater overdensities than SHARK and the star formation prescription that are driving differences in the resulting stellar mass and SFR distributions.

6.2 The onset of quenching in massive galaxies

Another important difference between the simulations is their predictions on the onset of quenching in massive galaxies, $\geq 10^{10} M_{\odot}$ as indicated by the prevalence of the turn over and increased scatter in the SFS shown in Figures 4 to 6. Davies et al. (2022) interpreted the increased scatter at the massive end of the SFS for the DEVILS sample as being caused by AGN feedback inhibiting star formation and driving galaxies below the SFS. This is corroborated by earlier EAGLE simulations' results of Katsianis et al. (2019), who also attributed the increased scatter at the massive end to AGN feedback.

Here, we explore much higher redshifts than Davies et al. (2022) ($0.1 < z < 0.85$) and Katsianis et al. (2019) ($z < 4$). To investigate the effect of AGN feedback on quenching and the increased scatter in the SFS at the high-mass end we show the distance from the SFS as a function of super massive black hole (SMBH) mass for the two simulations in Figure 9. We use the sSFR per unit mass shifted up by the median sSFR between $M_{\text{BH}} = 10^{6.75} \rightarrow 10^{7.25} M_{\odot}$ as a proxy measure for distance to the SFS. We use this measure instead of our fits to the SFS to promote comparisons with lower redshift results for which we do not have SFS fits. We see that the $\Delta\text{SFS} \sim 0$ is approximately constant, in SHARK over all black hole masses at all redshifts. We see at $z \lesssim 9$ that the ΔSFS between SHARK and FLARES begins to diverge with FLARES experiencing a downturn in ΔSFS for SMBH masses $M_{\text{BH}} \gtrsim 10^7 M_{\odot}$. The divergence for $M_{\text{BH}} \gtrsim 10^7 M_{\odot}$ is greatest at $z \lesssim 7$ that lines up well with the similar redshifts where

the turn over and increased scatter become more prevalent in FLARES compared to SHARK, indicating a connection between forming very massive SMBHs and quenching, congruous with the lower redshift conclusions in the literature. Bower et al. (2017) showed that in EAGLE, galaxies being quenched by AGN feedback are characterised by a strongly non-linear SMBH growth phase. The SMBH mass is thus a good predictor of the regime in which AGN feedback is efficient. Terrazas et al. (2020) showed that in another cosmological hydrodynamic simulation, ILLUSTRIS-TNG, a similar behaviour is seen, and galaxies above a given SMBH mass experience AGN feedback quenching.

The dashed and dotted lines in Figure 9 show the $z = 0$ and $z = 2$ relations respectively for EAGLE AGNdT9-50 and SHARK. We remind the reader that FLARES adopted the same model as EAGLE meaning the latter is the right comparison dataset for FLARES at $z < 5$. The EAGLE Ref-100 simulation uses a different set of parameters meaning that it is unsuitable for comparison despite being a larger volume. At $z = 0$, both EAGLE and SHARK predict a sharp downturn in sSFR around $M_{\text{BH}} \gtrsim 10^7 M_{\odot}$ indicating that above this SMBH mass AGN feedback becomes efficient at inhibiting star formation in galaxies. This SMBH mass threshold for quenching does not evolve in EAGLE and FLARES, staying around $M_{\text{BH}} \gtrsim 10^7 M_{\odot}$ at all times; i.e., as soon as a galaxy hits that SMBH, its star formation activity starts to quench due to AGN feedback. This is highlighted by the orange X and diamond symbols that correspond to the black hole mass at which the ΔSFS experiences its sharpest down turn at $z = 2$ and $z = 0$ respectively. Note, that the position of these symbols are identical. However, SHARK behaves very differently, with the SMBH threshold mass above which quenching driven by AGN feedback happens evolves towards higher SMBH masses as the redshift increases. By $z = 2$, the SMBH mass threshold for quenching in SHARK is ~ 1 dex higher than at $z = 0$ as indicated by the blue X and diamond symbols respectively.

In SHARK the SMBH accretion rate due to hot halo cooling is what regulates the efficiency of star formation quenching in central galaxies (Lagos et al. 2018). We observe a greater variation in turn over mass over time in SHARK that is a reflection of the AGN entering the appropriate feedback mode at different SMBH masses at different redshifts. This is not the case in EAGLE and FLARES, and quenching mostly occurs at a fixed mass. This implies that the AGN in SHARK for $z \geq 5$ are mostly growing in the QSO mode, and are yet to have significant accretion rates from the hot-halo cooling mode. This means they cannot quench galaxies, while all that matters in FLARES is that the AGN have grown to sufficient masses, which happens at $z \lesssim 7$. Therefore, the cause of the difference seen in the SFS at the massive end between the simulations is a result of different models of AGN feedback. The JWST will be able to probe the SFS up to $M_{\star} \sim 10^{10} M_{\odot}$, providing stringent constraints on theoretical models of AGN feedback.

6.3 Dust attenuation differences

We have established that the two simulations model the assembly of stellar mass similarly; however, the differences in the treatment of dust and attenuation in the simulations yields quite different predictions of the number of galaxies that are currently observable by HST (Fig. 1).

Figure 10 shows the median A_{FUV} of galaxies in the SFR - M_{\star} plane at $z = 6, 8, 10$ for FLARES (top) and SHARK (bottom), where the FUV attenuation is calculated as

$$A_{\text{FUV}} = -2.5 \log_{10}(\text{FUV}_{\text{obs}}/\text{FUV}_{\text{intr}}). \quad (11)$$

Here, FUV_{obs} is the FUV flux observed through the dusty medium

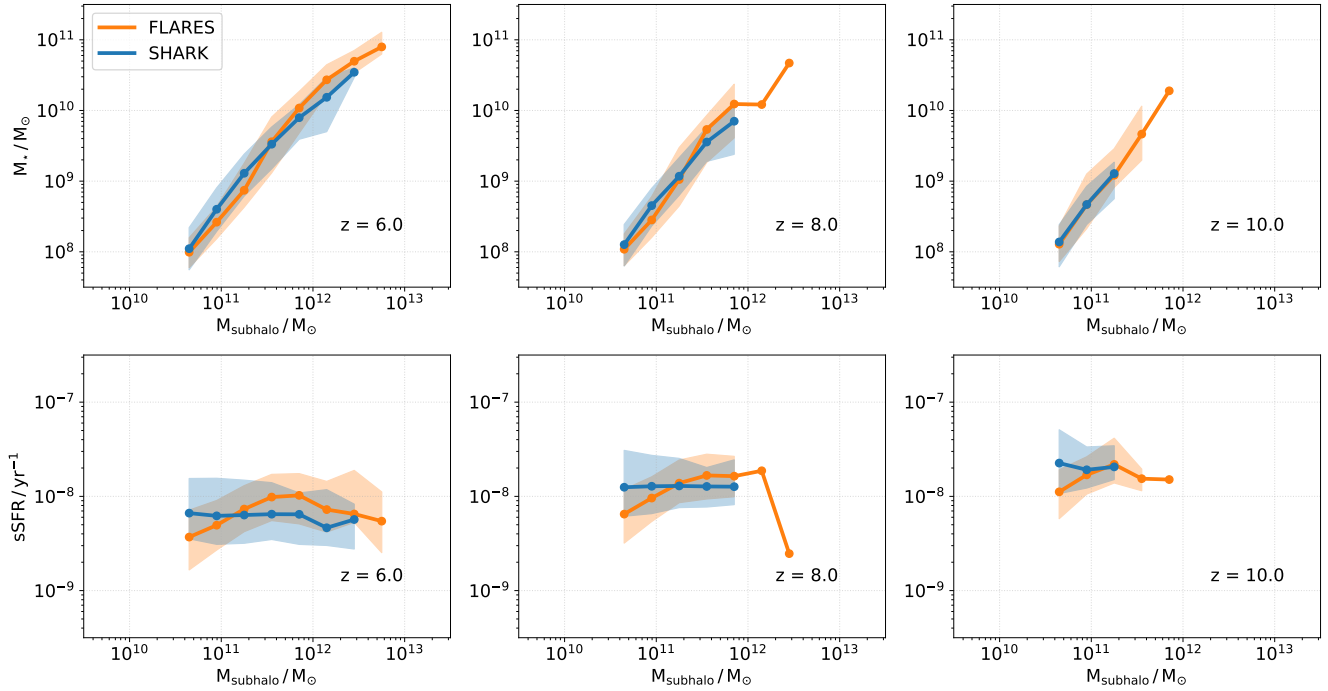


Figure 8. *Top:* $M_{\text{subhalo}} - M_{\star}$ at $z = 6, 8, 10$, as labelled, for FLARES (orange) and SHARK (blue). The dotted lines show the median quantity while the shaded regions show the 5-95 quantiles. We only show central galaxies here. *Bottom:* $s\text{SFR} - M_{\text{subhalo}}$. The colours and labels are the same as the top row. We only show central galaxies here.

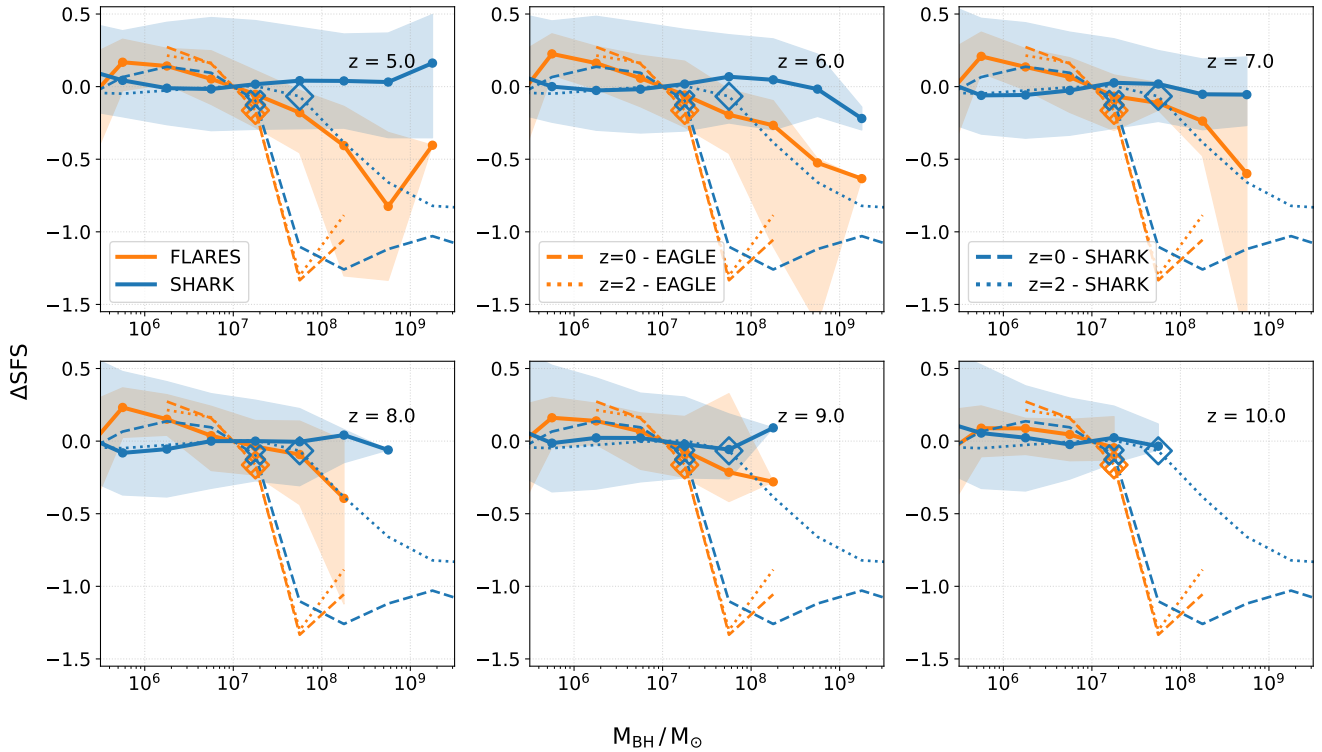


Figure 9. $\Delta\text{SFS} - M_{\text{BH}}$ at redshifts $z = 5, 6, 7, 8, 9, 10$ as labelled for FLARES (orange) and SHARK (blue). We use the $s\text{SFR}$ per unit black hole mass shifted up by the median $s\text{SFR}$ between $M_{\text{BH}} = 10^{6.75} \rightarrow 10^{7.25} M_{\odot}$ as a proxy measure for distance to the SFS. The solid lines indicate the median and the shaded regions indicate 16-84 quantiles. The dashed and dotted lines show the results at $z = 0$ and $z = 2$, where we show results from the EAGLE-AGNt9-50 simulation in place of FLARES. The X symbols indicate the black hole mass at which ΔSFS experiences its greatest decline at $z = 2$, while the diamond symbols indicate the same thing but for $z = 0$. Note that for EAGLE, the Xs and diamonds positions are identical.

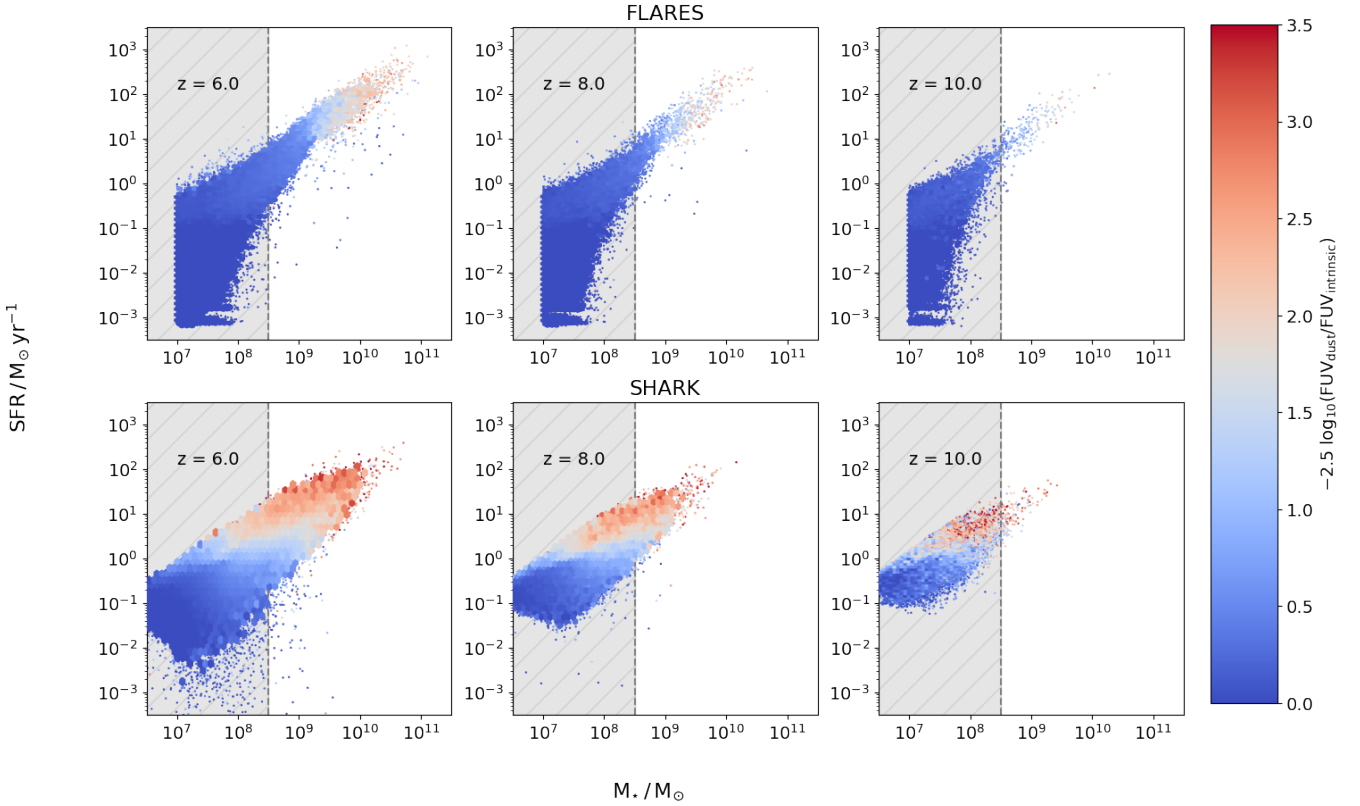


Figure 10. SFR – M_{\star} at redshifts $z = 6, 8, 10$ for FLARES (above) and SHARK (below). We discretised the plane into hexagonal bins of equal area, and colour them according to the median FUV attenuation in each. Each bin contains a minimum of 5 objects. The scale is shown in the colour bar on the right. Points indicate single galaxies with the same colour scheme indicating their attenuation. The grey shaded regions show the approximate stellar mass resolution limit of $10^{8.5} M_{\odot}$.

and FUV_{intr} is the FUV flux before it has been attenuated by dust. Broadly, the attenuation in both simulations traces the SFS, with dustier galaxies inhabiting the top end of it, $M_{\star} \gtrsim 10^9 M_{\odot}$. However, the attenuation gradient tracks more closely with stellar mass in FLARES, whereas it tracks more so with SFR in SHARK, for all redshifts shown here. In addition, SHARK yields higher values of A_{FUV} for the most star-forming and massive galaxies in the simulation, compared to FLARES. This is related to the instantaneous chemical enrichment model adopted in SHARK which allows very starbursting galaxies to enrich their ISM with metals very quickly compared to FLARES, where a delay is applied. This corroborates the differences in the CSMH and CSFRH between the two simulations that was discussed in section 5. Because both simulations use the gas mass in metals as proxies for the dust content of galaxies, it is clear that the chemical enrichment model plays a critical role in the predicted dust attenuation.

6.4 The volume probed by JWST surveys

So far we have not accounted for the survey volume required to ascertain a sample representative of the Universe. Uncertainties in pencil beam surveys such as the Hubble Ultra Deep Field (Beckwith et al. 2006) are dominated by cosmic variance where the probability of obtaining a survey sample representative of the entire Universe scales with area coverage (Driver & Robotham 2010).

To better assess the impact of survey area on the ability to constrain the shape of the SFS, we refit the SFS after resampling the stellar mass

and star formation rate distributions assuming some survey volume. Specifically, we calculate the 2D histogram of SFR and stellar mass per unit volume and for a given redshift for JWST-selected galaxies in both simulations, and calculate the cumulative distribution function per unit volume at $z = 5, 6, 7, 8, 9$ and 10 . Multiplying this by a given survey volume gives the expected cumulative number distribution of galaxies in the survey at a given redshift. Here, we do not assume any random errors on stellar masses or star formation rates to aid in comparison between fits from the same simulation. We repeat this resampling and fitting process ten times and average the derived SFS parameters to mitigate randomness caused by sampling the joint stellar mass and SFR distributions. We show the results in Figure 11 for the entire population of galaxies in both simulations, the JWST-detected galaxies (determined from their F200W apparent magnitude), galaxies detected in a single pointing of 10 arcmin^2 , galaxies detected in 220 arcmin^2 and galaxies detected in 0.7 deg^2 . The choice of 220 arcmin^2 and 0.7 deg^2 survey areas comes from the Webb Medium Deep Field (WMDf) Survey (Proposal ID: 1176, PI: R. Windhorst) and the Webb COSMOS survey (Proposal ID: 1727, PI: J. Kartaltepe)².

We see that in general it becomes more difficult to constrain the shape of the SFS with smaller area surveys. This is true in SHARK over all redshifts shown, while only at $z > 7$ in FLARES do single pointings struggle to constrain the SFS. The fact that all survey areas

² <https://www.stsci.edu/jwst/science-execution/program-information.html>

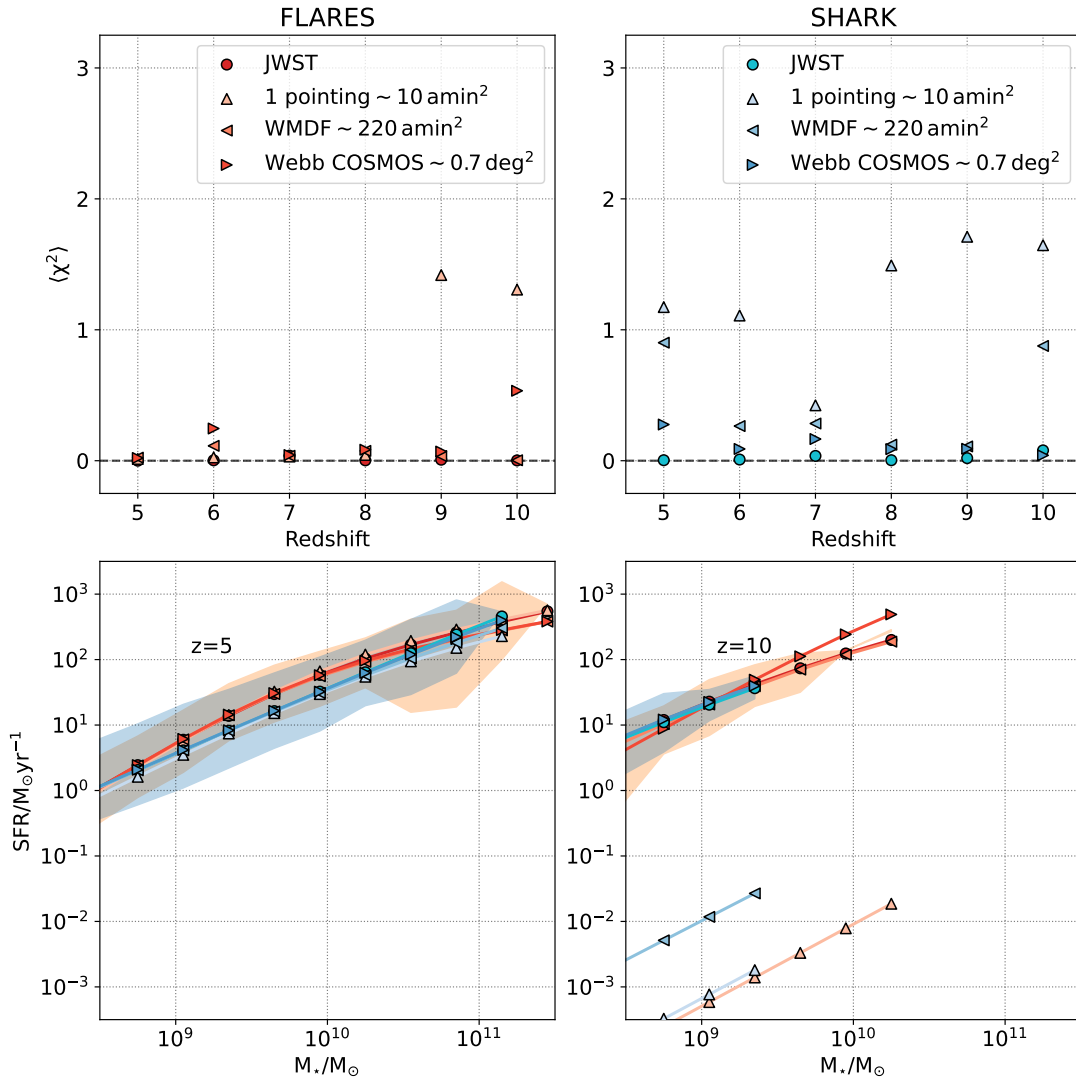


Figure 11. *Top:* Averaged χ^2 values for each of the SFS fits where we have resampled galaxy stellar masses and SFRs according to different survey volumes 10 times for FLARES (left) and SHARK (right). $\chi^2 = \sum_{i=0}^4 \frac{(x_i - x_i^{\text{true}})^2}{x_i^{\text{true}}}$ where x_i represents the derived parameters of the resampled SFS and x_i^{true} the derived parameters for the entire population in the simulations. Filled circles show the χ^2 for the JWST-detected galaxies; upright, left-pointing and right-pointing triangles show the χ^2 for a JWST surveys of areas 10 amin^2 (i.e. a single pointing), 220 amin^2 (i.e. a medium deep field) and 0.7 deg^2 (i.e. the Webb COSMOS survey), respectively, as labelled. *Bottom:* SFS plots at $z=5$ (left) and $z=10$ (right), for FLARES (red and orange colours) and SHARK (blue and cyan colours). We use the same symbols and colour gradient as the top panels to reflect different fits for each sample. Orange and blue shaded regions show the 5th – 95th percentile ranges for all galaxies in the simulations.

can constrain the SFS in FLARES at $z \sim 5$ while SHARK can not is a reflection of the two component SFS function being unsuitable for SHARK at these lower redshifts. We do see that both simulations predict that a Webb COSMOS-like survey without any assumed random errors will be able to constrain the true SFS parameters at $z \geq 5$. We further explore the effect of random errors on M_\star and SFR in appendix A. Nevertheless, we advocate for wider area surveys that will be able to get accurate SFRs and stellar masses needed to thoroughly study the SFS.

Interestingly, at $z=6, 10$ in FLARES the average χ^2 for the Webb COSMOS-like survey is higher than the narrower WMDF-like survey. This is likely a result of the fitting technique. At $z=10$ for example, the turn over mass is $10^{10} M_\odot$ for the WMDF-like survey, which goes beyond the range of resampled galaxies implying that the turnover is unphysical. For the Webb COSMOS-like survey, we

predict more galaxies at higher stellar mass, but not so many that the turn over in the SFS can be constrained. In this case, the SFS favours a single power law fit, and the average χ^2 increases. This just further shows why it is necessary to have accurate SFRs and stellar masses over the breadth of the SFR – M_\star .

Our resampling method does not take into account the underlying structure of the Universe that will affect our predicted constraints on the SFS. As FLARES is comprised of 40 unique subvolumes that have each been accordingly weighted, a smooth mass distribution cannot be reconstructed, and thus cannot be used to test cosmic variance directly. Therefore, to test the effect of cosmic variance, we limit our attention to SHARK, where we can partition the box into smaller subvolumes of equal weighting and refit the SFS in each. We divide the whole SHARK box in 3 dimensions into 8 independent, contiguous

and equal size subvolumes. We, once again, choose not to use random errors to emphasise the effect of cosmic variance only.

Figure 12 shows the resulting SFS of this exercise. Cosmic variance mildly impacts the ability to constrain the SFS at all redshifts. At $z = 5$ cosmic variance negligibly affects the SFS fit. By $z = 10$ cosmic variance affects the whole appearance of the SFS, with the effect on the constraint at high masses being significant. Therefore, in addition to our advocacy of wider surveys we further advocate for surveys distributed over a range of fields and sight lines.

7 CONCLUSIONS

We have presented predictions on the ability for the JWST to quantify the details of star formation and stellar mass assembly of galaxies between $z = 5 \rightarrow 10$. By using two distinct simulations, FLARES and SHARK, we have provided a theoretical framework, unmarred by potential systematic biases contained in a single simulation, in which the emerging observations of the JWST can be tested to better understand the astrophysics of the early Universe.

The key results are:

- **Stellar mass and SFR functions:** We predict that throughout redshifts $z = 6 \rightarrow 10$, the JWST will be able to detect all intrinsically bright galaxies up to redshift $z = 10$, and thus will be able to parametrise the distributions of stellar mass and SFRs of the first galaxies in the Universe. Conversely, both FLARES and SHARK predict that very dust-obscured galaxies are completely absent from current HST surveys. This is expected to affect current measurements of the SMF and SFRF from HST observations (Katsianis et al. 2017; McLure et al. 2010; Bouwens et al. 2015; Song et al. 2016; González et al. 2011; Thorne et al. 2021; Stefanon et al. 2021). We predict that the JWST observations are only limited by the detection sensitivity of the instrument and will not miss highly obscured galaxies.

- **Star forming main sequence:** We predict that the JWST will be able to parametrise the shape and the stellar mass dependent scatter of the SFS between $z = 5 \rightarrow 10$ for the first time by obtaining observations over a sufficient wide range of stellar masses and SFRs. As the SFS encodes information about the astrophysics driving the shape and scatter the JWST should prove to be an invaluable tool in improving our understanding of galaxy formation up to the onset of cosmic reionisation when the first galaxies formed, and on the rising of massive, AGN-quenched galaxies towards the end of reionisation.

- **Cosmic stellar and SFR histories:** We predict that the JWST will be able to observe every intrinsically bright galaxy out to redshift $z \sim 10$. The only limit of the instrument will be that of sensitivity and area. This is an improvement upon existing short-wavelength surveys that potentially miss the dustiest galaxies in the Universe. As such, the JWST should be able to constrain the CSMH and CSFRH between $z = 5 \rightarrow 10$ robustly.

- **The dependence of prediction on the baryon physics models:** By using two independent simulations we have shown that each prediction on the ability of the JWST is model dependent. We have shown that both FLARES and SHARK show similar distributions of stellar mass and SFR indicating that their sub-grid recipes are similar, but not exact. An important delineator between the two simulations is how each models dust that is itself sensitive to how each simulation deals with star formation and chemical enrichment. As we predict that the JWST will be able to provide a sufficient census of galaxies out to redshift $z \sim 10$ we suggest that the JWST observations, in combination with multi-wavelength follow up observations, will be able distinguish between the two models.

- **The effect of survey area and cosmic variance:** By sampling from our simulated galaxy populations to obtain particular survey samples we find that wide area surveys are necessary to constrain the shape of the star forming main sequence from $z = 5$ to $z = 10$. Furthermore, by dividing the SHARK box into 8 independent and contiguous subvolumes and refitting the SFS in each we show that cosmic variance is an important factor in influencing the shape of the SFS at $z \sim 10$.

With continued observations, the JWST will open the door to the next milestone toward our understanding of galaxy formation. We have presented predictions on the ability of the JWST so that we are well poised to compare them against the JWST observations as they continue to arrive. A deeper study of the specific sub-grid recipes used in simulations will allow us to interpret the astrophysics that the telescope recovers. Although FLARES and SHARK broadly agree with each other, it is a key objective of the JWST to distinguish, and comprehend the origin of, the slight differences between the independent models.

ACKNOWLEDGEMENTS

JCJD is supported by an Australian Government Research Training Program (RTP) Scholarship. We thank the entire FLARES team for their support and feedback. CL has received funding from the ARC Centre of Excellence for All Sky Astrophysics in 3 Dimensions (ASTRO 3D), through project number CE170100013. LJMD acknowledges support from the Australian Research Councils Future Fellowship scheme (FT200100055). CCL acknowledges support from the Royal Society under grant RGF/EA/181016. Cosmic Dawn Centre is funded by the Danish National Research Foundation. This work was supported by resources provided by The Pawsey Supercomputing Centre with funding from the Australian Government and the Government of Western Australia. This work used the DiRAC@Durham facility managed by the Institute for Computational Cosmology on behalf of the STFC DiRAC HPC Facility (www.dirac.ac.uk). The equipment was funded by BEIS capital funding via STFC capital grants ST/K00042X/1, ST/P002293/1, ST/R002371/1 and ST/S002502/1, Durham University and STFC operations grant ST/R000832/1. DiRAC is part of the National e-Infrastructure.

DATA AVAILABILITY

Figures, scripts and additional data is available upon reasonable request to the authors. FLARES is hosted here <https://github.com/flaresimulations> and SUBFIND/photometry outputs are available here <https://flaresimulations.github.io/>. SHARK is hosted here <https://github.com/ICRAR/shark>. SHARK SUBFIND/photometry outputs are available upon reasonable request.

REFERENCES

- Abramson L. E., Kelson D. D., Dressler A., Poggianti B., Gladders M. D., Oemler Augustus J., Vulcani B., 2014, *ApJ*, **785**, L36
 Bahé Y. M., et al., 2017a, *MNRAS*, **470**, 4186–4208
 Bahé Y. M., et al., 2017b, *MNRAS*, **470**, 4186–4208
 Barnes D. J., et al., 2017, *MNRAS*, **471**, 1088
 Baugh C. M., 2006, *Reports on Progress in Physics*, **69**, 3101
 Beckwith S. V. W., et al., 2006, *AJ*, **132**, 1729

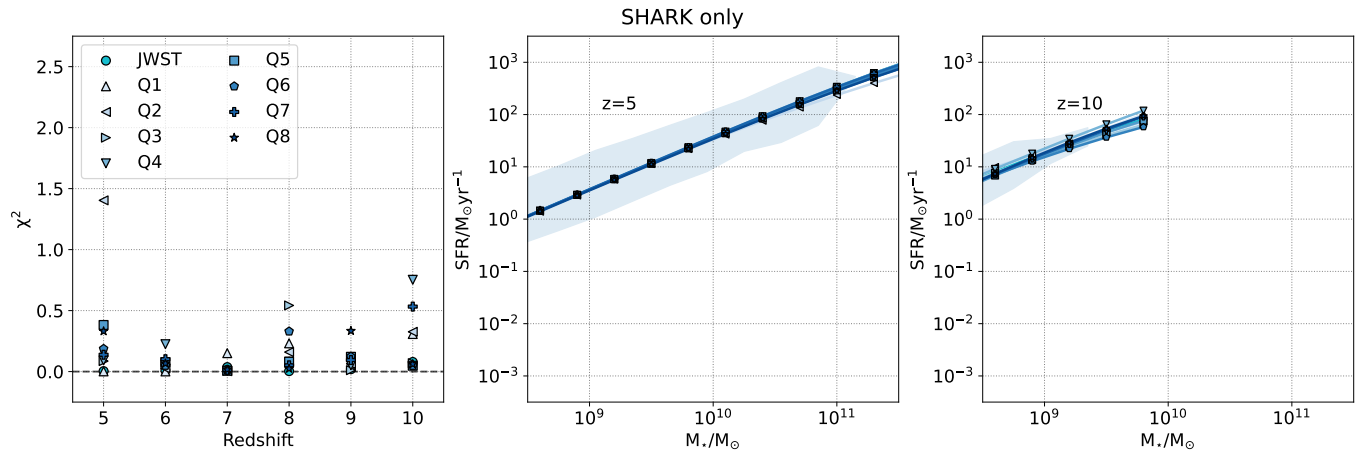


Figure 12. *Left:* χ^2 values (as defined in Figure 11), for the SFS fit performed in each subvolumes of the total SHARK box. Galaxies selected based on their F200W magnitude, are shown with filled circles. We show each set of 8 subvolumes with different symbols, as labelled. *Middle and right:* SFS plots at $z = 5$ (middle) and $z = 10$ (right). We use the same symbols and colour gradient as the left panels to show the SFS fits of each galaxy sample.

Bellstedt S., et al., 2020, *Monthly Notices of the Royal Astronomical Society*, 498, 5581

Benson A. J., 2010, *Phys. Rep.*, 495, 33

Bouwens R. J., et al., 2012, *ApJ*, 752, L5

Bouwens R. J., et al., 2015, *ApJ*, 803, 34

Bouwens R., et al., 2020, *The Astrophysical Journal*, 902, 112

Bouwens R. J., et al., 2021, *The Astronomical Journal*, 162, 47

Bower R. G., Schaye J., Frenk C. S., Theuns T., Schaller M., Crain R. A., McAlpine S., 2017, *MNRAS*, 465, 32

Brinchmann J., Charlot S., White S. D. M., Tremonti C., Kauffmann G., Heckman T., Brinkmann J., 2004, *MNRAS*, 351, 1151

Bruzual G., Charlot S., 2003, *MNRAS*, 344, 1000

Cañas R., Elahi P. J., Welker C., del P Lagos C., Power C., Dubois Y., Pichon C., 2019, *MNRAS*, 482, 2039

Camps P., Baes M., 2015, *Astronomy and Computing*, 9, 20

Casey C. M., Narayanan D., Cooray A., 2014, *Physics Reports*, 541, 45–161

Casey C. M., et al., 2018, *ApJ*, 862, 77

Chabrier G., 2003, *PASP*, 115, 763

Charlot S., Fall S. M., 2000, *ApJ*, 539, 718

Cole S., Lacey C. G., Baugh C. M., Frenk C. S., 2000, *MNRAS*, 319, 168

Cook R. H. W., Cortese L., Catinella B., Robotham A., 2020, *MNRAS*, 493, 5596

Crain R. A., et al., 2015, *MNRAS*, 450, 1937–1961

Croton D. J., 2013, *Publ. Astron. Soc. Australia*, 30

Croton D. J., et al., 2016, *ApJS*, 222, 22

Curtis-Lake E., Chevillard J., Charlot S., Sandles L., 2021, *MNRAS*, 503, 4855

Davies L. J. M., et al., 2016, *MNRAS*, 461, 458

Davies L. J. M., et al., 2018, *MNRAS*, 480, 768

Davies L. J. M., et al., 2019, *MNRAS*, 483, 1881

Davies L. J. M., et al., 2021, *MNRAS*, 506, 256

Davies L. J. M., et al., 2022, *MNRAS*, 509, 4392

Davis M., Efstathiou G., Frenk C. S., White S. D. M., 1985, *ApJ*, 292, 371

De Vis P., et al., 2019, *Astronomy & Astrophysics*, 623, A5

Draine B. T., 2003, *ARA&A*, 41, 241

Driver S. P., Robotham A. S. G., 2010, *MNRAS*, 407, 2131

Elahi P. J., Welker C., Power C., Lagos C. d. P., Robotham A. S. G., Cañas R., Poulton R., 2018, *MNRAS*, 475, 5338

Elahi P. J., Cañas R., Poulton R. J. J., Tobar R. J., Willis J. S., Lagos C. d. P., Power C., Robotham A. S. G., 2019a, *Publ. Astron. Soc. Australia*, 36

Elahi P. J., Poulton R. J. J., Tobar R. J., Cañas R., Lagos C. d. P., Power C., Robotham A. S. G., 2019b, *Publ. Astron. Soc. Australia*, 36, e028

Eldridge J. J., Stanway E. R., Xiao L., McClelland L. A. S., Taylor G., Ng M., Greis S. M. L., Bray J. C., 2017, *Publ. Astron. Soc. Australia*, 34, e058

Finkelstein S. L., et al., 2015, *ApJ*, 810, 71

Foreman-Mackey D., Hogg D. W., Lang D., Goodman J., 2013, *PASP*, 125, 306

Fudamoto Y., et al., 2021, *Nature*, 597, 489–492

Furlong M., et al., 2015, *MNRAS*, 450, 4486

Gardner J. P., et al., 2006, *Space Sci. Rev.*, 123, 485

González V., Labbé I., Bouwens R. J., Illingworth G., Franx M., Kriek M., 2011, *ApJ*, 735, L34

Grogin N. A., et al., 2011, *ApJS*, 197, 35

Hao C.-N., Kennicutt R. C., Johnson B. D., Calzetti D., Dale D. A., Moustakas J., 2011, *ApJ*, 741, 124

Katsianis A., et al., 2017, *MNRAS*, 472, 919

Katsianis A., et al., 2019, *ApJ*, 879, 11

Koekemoer A. M., et al., 2007, *ApJS*, 172, 196

Koushan S., et al., 2021, *Monthly Notices of the Royal Astronomical Society*, 503, 2033

Kregel M., van der Kruit P. C., de Grijs R., 2002, *MNRAS*, 334, 646

Krumholz M. R., McKee C. F., Tumlinson J., 2009, *ApJ*, 699, 850–856

Labbé I., et al., 2013, *ApJ*, 777, L19

Lagos C. D. P., Lacey C. G., Baugh C. M., Bower R. G., Benson A. J., 2011, *MNRAS*, 416, 1566

Lagos C. D. P., Baugh C. M., Zwaan M. A., Lacey C. G., Gonzalez-Perez V., Power C., Swinbank A. M., van Kampen E., 2014, *MNRAS*, 440, 920

Lagos C. d. P., Tobar R. J., Robotham A. S. G., Obreschkow D., Mitchell P. D., Power C., Elahi P. J., 2018, *MNRAS*, 481, 3573

Lagos C. d. P., et al., 2019, *MNRAS*, 489, 4196

Lee K.-S., et al., 2012, *ApJ*, 752, 66

Lee N., et al., 2015, *ApJ*, 801, 80

Leslie S. K., et al., 2020, *ApJ*, 899, 58

Lilly S. J., Carollo C. M., Pipino A., Renzini A., Peng Y., 2013, *ApJ*, 772, 119

Lovell C. C., Vijayan A. P., Thomas P. A., Wilkins S. M., Barnes D. J., Irodotou D., Roper W., 2021, *MNRAS*, 500, 2127

Madau P., Dickinson M., 2014, *ARA&A*, 52, 415

Mathis J. S., Rumpf W., Nordsieck K. H., 1977, *ApJ*, 217, 425

Matthee J., Schaye J., 2019, *MNRAS*, 484, 915

McLure R. J., Dunlop J. S., Cirasuolo M., Koekemoer A. M., Sabbi E., Stark D. P., Targett T. A., Ellis R. S., 2010, *MNRAS*, 403, 960

Meurer G. R., Heckman T. M., Calzetti D., 1999, *ApJ*, 521, 64

Michałowski M. J., Hayward C. C., Dunlop J. S., Bruce V. A., Cirasuolo M., Cullen F., Hernquist L., 2014, *A&A*, 571, A75

Navarro J. F., Frenk C. S., White S. D. M., 1997, *ApJ*, 490, 493–508

Noeske K. G., et al., 2007a, *ApJ*, 660, L43

Noeske K. G., et al., 2007b, *ApJ*, 660, L47

Oesch P. A., Bouwens R. J., Illingworth G. D., Labbé I., Stefanon M., 2018, *ApJ*, 855, 105

- Pearson W. J., et al., 2018, *A&A*, 615, A146
- Planck Collaboration et al., 2014, *A&A*, 571, A1
- Planck Collaboration et al., 2016, *A&A*, 594, A13
- Rémy-Ruyer A., et al., 2014, *A&A*, 563, A31
- Rigby J., et al., 2022, Characterization of JWST science performance from commissioning, <http://arxiv.org/abs/2207.05632>
- Robotham A. S. G., Bellstedt S., Lagos C. d. P., Thorne J. E., Davies L. J., Driver S. P., Bravo M., 2020, *MNRAS*, 495, 905
- Salim S., et al., 2007, *ApJS*, 173, 267
- Schaller M., Dalla Vecchia C., Schaye J., Bower R. G., Theuns T., Crain R. A., Furlong M., McCarthy I. G., 2015, *MNRAS*, 454, 2277
- Schaye J., et al., 2010, *MNRAS*, 402, 1536
- Schaye J., et al., 2015, *MNRAS*, 446, 521
- Schenker M. A., et al., 2013, *ApJ*, 768, 196
- Shen X., Vogelsberger M., Nelson D., Tacchella S., Hernquist L., Springel V., Marinacci F., Torrey P., 2021, arXiv e-prints, p. [arXiv:2104.12788](https://arxiv.org/abs/2104.12788)
- Somerville R. S., Davé R., 2015, *ARA&A*, 53, 51
- Song M., et al., 2016, *ApJ*, 825, 5
- Speagle J. S., Steinhardt C. L., Capak P. L., Silverman J. D., 2014, *ApJS*, 214, 15
- Springel V., 2005, *MNRAS*, 364, 1105–1134
- Springel V., White S. D. M., Tormen G., Kauffmann G., 2001, *MNRAS*, 328, 726
- Springel V., et al., 2005, *Nature*, 435, 629
- Stanway E. R., Eldridge J. J., 2018, *Monthly Notices of the Royal Astronomical Society*, 479, 75
- Stefanon M., Bouwens R. J., Labbé I., Illingworth G. D., Gonzalez V., Oesch P. A., 2021, *ApJ*, 922, 29
- Tacchella S., Dekel A., Carollo C. M., Ceverino D., DeGraf C., Lapiner S., Mandelker N., Primack Joel R., 2016, *MNRAS*, 457, 2790
- Terrazas B. A., et al., 2020, *MNRAS*, 493, 1888
- Thorne J. E., et al., 2021, *MNRAS*, 505, 540
- Trayford J. W., Lagos C. d. P., Robotham A. S. G., Obreschkow D., 2020, *MNRAS*, 491, 3937
- Vazdekis A., Koleva M., Ricciardelli E., Röck B., Falcón-Barroso J., 2016, *MNRAS*, 463, 3409
- Vijayan A. P., Clay S. J., Thomas P. A., Yates R. M., Wilkins S. M., Henriques B. M., 2019, *MNRAS*, 489, 4072
- Vijayan A. P., Lovell C. C., Wilkins S. M., Thomas P. A., Barnes D. J., Irodotou D., Kuusisto J., Roper W. J., 2021, *MNRAS*, 501, 3289
- Vijayan A. P., et al., 2022, *MNRAS*, 511, 4999
- Vogelsberger M., et al., 2014, *MNRAS*, 444, 1518
- Vogelsberger M., et al., 2020, *MNRAS*, 492, 5167
- Weigel A. K., Schawinski K., Bruderer C., 2016, *MNRAS*, 459, 2150
- Whitaker K. E., van Dokkum P. G., Brammer G., Franx M., 2012a, *ApJ*, 754, L29
- Whitaker K. E., van Dokkum P. G., Brammer G., Franx M., 2012b, *ApJ*, 754, L29
- Wilkins S. M., et al., 2022a, First Light And Reionisation Epoch Simulations (FLARES) V: The redshift frontier, <http://arxiv.org/abs/2204.09431>
- Wilkins S. M., et al., 2022c, First Light And Reionisation Epoch Simulations (FLARES) VI: The colour evolution of galaxies $z=5-15$, <http://arxiv.org/abs/2207.10920>
- Wilkins S. M., et al., 2022b, First Light And Reionisation Epoch Simulations (FLARES) VII: The Star Formation and Metal Enrichment Histories of Galaxies in the early Universe, <http://arxiv.org/abs/2208.00976>
- Wuyts S., et al., 2011, *ApJ*, 742, 96
- Yabe K., Ohta K., Iwata I., Sawicki M., Tamura N., Akiyama M., Aoki K., 2009, *ApJ*, 693, 507

APPENDIX A: EFFECT OF UNCERTAINTIES ON THE SFS FITTING

To investigate the effect of measurement uncertainties on the ability to recover the SFS parameters of the true galaxy population we refit

the SFS of the JWST population with varied Gaussian uncertainties added to the stellar masses and star formation rates. Figure A1 shows the relative error of the parameters of the SFS as a function of the assumed uncertainty on the stellar masses and star formation rates of the JWST detected populations in the simulations. The relative error is

$$\text{Relative error} = \left| \frac{X_{\text{JWST}} - X_{\text{All}}}{X_{\text{All}}} \right|, \quad (\text{A1})$$

where X_{JWST} are the parameters calculated for the JWST population with the absorbed uncertainties and X_{All} are the calculated parameters for the entire galaxy population in the simulations. When using the same prior distributions as those we used for the fitting in Figures 4 and 5 we found that for varied uncertainty combinations the relative error was largest in different parameters, making it difficult to see just how additive normal noise affected the fitting. For this reason, we fit the parameters independently, keeping the remaining three parameters fixed, with each uncertainty combination. We achieve this by using a uniform prior on the desired parameter and narrow normal priors centred on the true population parameters for the remaining three parameters, cycling through this process until all parameters have been considered. So for 7 uncertainty combinations, 4 parameters and 3 selected redshifts we perform $7 \times 4 \times 3 = 84$ MCMC fitting routines on each simulation.

Both simulations predict a similar trend of increased relative error on all parameters of the SFS as the uncertainty on the stellar masses star formation rates increases, as expected. Even with zero uncertainty there is a non-zero relative error indicating systematic offsets between the JWST detected and total galaxy populations in the simulations. This is perhaps unsurprising as the JWST will miss faint galaxies, and so the relationship between the total and JWST populations is not one-to-one. There is, in general, a larger increase in the relative error when the uncertainty on the stellar mass is increased from 0.2 dex to 0.4 dex compared to when the uncertainty on the SFR is increased from 0.2 dex to 0.4 dex to 0.6 dex. We thus suggest that accurate constraints on the stellar mass are more necessary to describe the SFS than constraints on SFR. The grey shaded regions shows the 10% margin. Beyond $\sim (0.2, 0.4)$ dex uncertainties on (M_{\star}, SFR) both simulations fail to recover the normalisation of the SFS to within 10% at all redshifts shown. For almost any uncertainty combination, the simulations are able to recover the turn over mass to within 10% at all redshifts except $z \sim 6$ in SHARK. The intermediate and high stellar mass slopes require far more accurate constraints on the stellar mass and SFR. Beyond ~ 0.2 dex and ≤ 0.6 dex uncertainty the intermediate stellar mass slope cannot be recovered to within 10% at all redshifts except $z = 6$ in FLARES. For most uncertainty combinations used in FLARES the high stellar mass slope can be recovered except beyond $\sim (0.2, 0.6)$ dex uncertainties on (M_{\star}, SFR) . On the other hand, for almost every uncertainty combination SHARK cannot recover the high stellar mass slope at all redshifts suggesting that the high stellar mass slope is subtle in SHARK by default. Interestingly, the apparent redshift dependencies on the recovery of these parameters appear to be reversed between the simulations, with FLARES showing decreasing relative error for the same uncertainty combination between $z = 10 \rightarrow 6$, whereas this is true between $z = 6 \rightarrow 10$ in SHARK. We do not comment any further on this in this work.

Some larger combinations of uncertainties result in a lower relative error than smaller uncertainties. For example, the $\sim (0.4, 0.6)$ dex combination is closer to the true population value of the turn over at all redshifts in SHARK than the $\sim (0.4, 0.2)$ combination is. This is more than likely a statistical effect or a symptom of the fitting

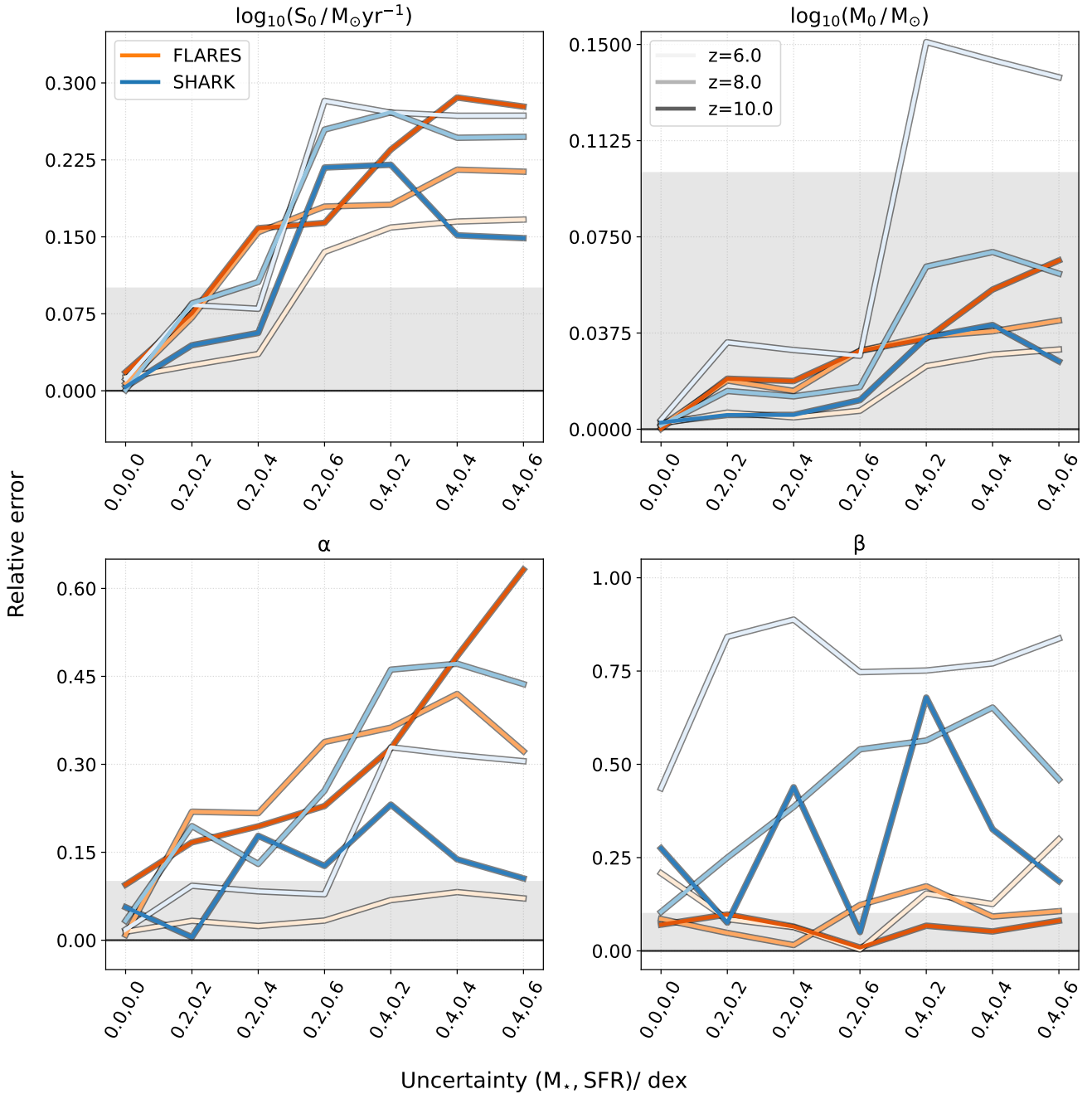


Figure A1. Relative error on each parameter, as labelled, used for fitting the SFS for the JWST population as a function of equal Gaussian uncertainty upon the stellar masses and star formation rates. Orange colours show the results for FLARES and blue colours show the results for SHARK. Each redshift, $z = 6, 8, 10$, is shown by a shading gradient with $z = 10$ being the darkest shade. The black line highlights no relative error, and the shaded region shows the 10% level.

routine as, intuitively, a larger uncertainty should result in worse agreement; though we do not investigate this further here. Ultimately, these trends show that poorer constraints on M_* and SFR result in a worse recovery of the true parameters of the SFS. These trends also provide an indication on the level of SFS accuracy that would be needed to adequately determine the true SFS to within 10%.

This paper has been typeset from a $\text{\TeX}/\text{\LaTeX}$ file prepared by the author.